A&A 674, A72 (2023)
https://doi.org/10.1051/0004-6361/202244777

Astronomy & Astrophysics

Imaging of the internal structure of an asteroid analogue from quasi-monostatic microwave measurement data

I. The frequency domain approach

A. Dufaure[1], C. Eyraud[1], L.-I. Sorsa[2], Y. O. Yusuf[1,2], S. Pursiainen[2], and J.-M. Geffrin[1]

[1] Aix-Marseille Univ, CNRS, Centrale Marseille, Institut Fresnel, Marseille, France
e-mail: astrid.dufaure@fresnel.fr
[2] Computing Sciences, Tampere University (TAU), PO Box 692, 33101 Tampere, Finland

Received 19 August 2022 / Accepted 1 March 2023

ABSTRACT

Context. The internal structure of small Solar System bodies (SSSBs) is still poorly understood, although it can provide important information about the formation process of asteroids and comets. Space radars can provide direct observations of this structure.
Aims. In this study, we investigate the possibility to infer the internal structure with a simple and fast inversion procedure applied to radar measurements. We consider a quasi-monostatic configuration with multiple measurements over a wide frequency band, which is the most common configuration for space radars. This is the first part (Paper I) of a joint study considering methods to analyse and invert quasi-monostatic microwave measurements of an asteroid analogue. This paper focuses on the frequency domain, while a separate paper focuses on time-domain methods.
Methods. We carried out an experiment in the laboratory equivalent to the probing of an asteroid using the microwave analogy (multiplying the wavelength and the target dimension by the same factor). Two analogues based on the shape of the asteroid 25143 Itokawa were constructed with different interiors. The electromagnetic interaction with these analogues was measured in an anechoic chamber using a multi-frequency radar and a quasi-monostatic configuration. The electric field was measured on 2372 angular positions (corresponding to a sampling offering complete information). We then inverted these data with two classical imaging procedures, allowing us to reach the structural information of the analogues interior. We also investigated reducing the number of radar measurements used in the imaging procedures, that is both the number of transmitter–receiver pairs and the number of frequencies.
Results. The results show that the 3D map of the analogues can be reconstructed without the need for a reference target. Internal structural differences are distinguishable between the analogues. This imaging can be achieved even with a reduced number of measurements. With only 35 well-selected frequencies over 321 and 1257 transmitter–receiver pairs, the reconstructions are similar to those obtained with the entire frequency band.

Key words. waves – scattering – methods: numerical – techniques: image processing – minor planets, asteroids: general

1. Introduction

In recent decades, humans have moved a step closer to understanding outer space through the development of new sensors and imaging techniques. Such discoveries make it possible to probe asteroids and comets, and thus improve our knowledge of the history and evolution of the Solar System (Herique et al. 2018). In particular, radar tomography constitutes a promising approach to reconstruct the internal structure of such small Solar System bodies (SSSBs). The Comet Nucleus Sounding Experiment by Radio-wave Transmission (CONSERT) radar, which probed comet 67P/Churyumov-Gerasimenko during the European Space Agency (ESA) Rosetta space mission (rendezvous in November 2014), is the first space radar sent to SSSBs (Kofman 2007). Thanks to this radar, many scientific discoveries have been made, such as the determination of the average permittivity, the volumetric dust/ice ratio, and the porosity of SSBBs (Kofman et al. 2015; Ciarletti et al. 2015, 2017; Herique et al. 2019a). These findings motivated the development of future space missions (Herique et al. 2018). The ESA HERA mission, which will be launched in October 2024 and will rendezvous with the binary asteroid 65803 Didymos in December 2026 (Michel et al. 2018), carries a monostatic radar called Juventas Radar (JuRa), which will be used to study the inner structure of Didymos (Herique et al. 2019b). Other potential missions equipped with space radars are also being considered for imaging asteroids, such as the near-Earth asteroid 99942 Apophis (Herique et al. 2022).

In order to prepare the measurement exploitation for these future space-radar missions, we investigate potential imaging procedures that can be used to reconstruct the interior of an asteroid. To do so, we prepared 3D printed analogues and measured the interaction of a multi-frequency electromagnetic wave within these analogues. These experiments were carried out in the laboratory in an anechoic chamber. The measurements were performed in a quasi-monostatic configuration, that is, a transmitter–receiver pair, which measures the scattered field, was moved close together on a spherical surface centred on the analogue. This data set was jointly processed with two inversion methods: one in the time domain and the other in the frequency domain. This latter is the subject of this paper and Paper I of the joint study.

Imaging procedures have been developed by the inverse problems community over the last decade. A review of 3D

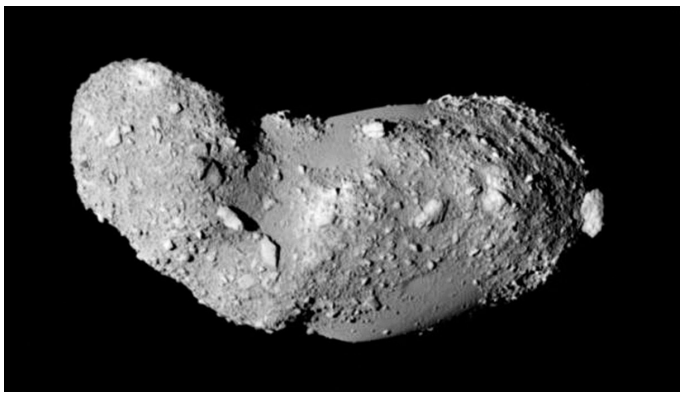

Fig. 1. Greyscale photography of the asteroid 25143 Itokawa taken by the European Southern Observatory (ESO).

inverse full-wave algorithms tested against the same experimental data set can be found in the special section devoted to inverse problems in 3D Fresnel database (Geffrin et al. 2009). These non-linear procedures allow a permittivity map to be retrieved for the probed target. The usual diameter of targets that are reconstructed with this type of non-linear procedure is of a few wavelengths (Litman & Crocco 2009). Finding a reconstruction for unusually large targets poses a challenge, because for 3D targets, the number of unknowns increases rapidly with the size of the target; although this number depends on the mathematical description of the unknowns (Deng et al. 2021b), it generally becomes very large for objects larger than a few wavelengths. Another difficulty is the noise that can disturb the measurements, because this type of procedure generally uses a minimisation process and can fall into a local minimum, especially in the presence of reduced signal-to-noise ratio (S/N). Different regularisation methods have been developed to avoid these problems, such as adding a penalty term (Bertero & Boccacci 1998), balancing each measurement according to its accuracy with a Bayesian approach (Eyraud et al. 2009), enforcing sparsity (Bevacqua et al. 2017), or combining methods (Deng et al. 2021a). In any case, significant methodological and computational developments are required in order to use this kind of procedure to image asteroid-sized objects.

Under certain assumptions, imaging procedures can be linearised by limiting the reconstruction process to finding a structural image for the target. In this type of non-iterative imaging procedure, the number of unknowns is less critical, and such procedures are also less sensitive to noise. In this study, we focus on adapting an approach of this kind in order to image SSSBs, or more specifically an asteroid analogue with the shape of 25143 Itokawa (see Fig. 1), (Fujiwara et al. 2006) with an internal structure made up of three layers, which was initially presented in Sorsa et al. (2019) and later fabricated as an analogue object (Sorsa et al. 2021a).

The standard synthetic aperture radar (SAR) imaging method is a classical technique applicable to a large target. The images resulting from SAR processing are projections of the reflectivity of a 3D volume onto a 2D surface (Curlander & McDonough 1991). This can lead to distortions in the reconstructed images. To obtain more coherent information on the height of the object, techniques have been developed such as interferometry SAR (Ulander & Frolind 1998) or polarimetry SAR (Cloude & Papathanassiou 1998). SAR tomography, which was developed in recent years (Reigber & Moreira 2000), is relevant to the imaging of SSSBs, and small asteroids in particular; see for example the advanced methods proposed in Gassot et al. (2021). Other techniques, also derived from radar imaging, have been developed such as wavefield tomography (Sava & Asphaug 2018b), which reconstructs the radar wave propagation speed at any point inside the object or wavefield migration (Sava & Asphaug 2018a), which provides images of the reflectors inside the body.

In this paper, we attempt to adapt an imaging procedure based on the reconstruction of the induced currents (Eyraud et al. 2013). The induced currents of the body area are obtained from scattered far-field using the observation equation of the scattered field in Eq. (1), which links the induced current to the scattered field. Our previous works were conducted using a single frequency and making the best use of spatial information in a bistatic configuration (Eyraud et al. 2018). In this study, we consider the most commonly used type of space radar, in a quasi-monostatic configuration, and exploit the multi-frequency aspect.

In Sect. 2, we present and describe the asteroid analogues, and in Sect. 3, we explain the measurements we carried out in the laboratory. The principles of inverse procedures and their implementation are detailed in Sect. 4. In Sect. 5, we explain strategies for reducing the number of measurements in both the number of spatial positions and the number of frequencies. The imaging results obtained in different cases are presented and discussed in Sect.s 6, and 7 is dedicated to our conclusions.

2. Asteroid analogue

In this study, we consider analogue models with the shape of asteroid 25143 Itokawa (Fig. 1) which was explored by the space mission Hayabusa (Kramer 2016; Tsuchiyama et al. 2011). Itokawa is an S-type Apollo asteroid discovered in 1998 by LINEAR, the Lincoln Near-Earth Asteroid Research joint project with the US Air Force, NASA, and the Massachusetts Institute of Technology, MIT, Lincoln Laboratory. The structure of Itokawa is composed of two parts, the head and the body, and due to its low density and large porosity this object is considered to be a 'rubble pile' asteroid (Fujiwara et al. 2006). In the present study, we analyse two 3D-manufactured analogue models with the shape of Itokawa in a controlled environment. Our aim is to reconstruct its interior structure from radar measurements and thus prepare for future space missions. The exterior surface of the analogue models is based on Hayabusa's accurate optical shape data (Kramer 2016). The analogues were manufactured using the low-loss Preperm ABS450 filament (Premix Oy, Finland) the relative electric permittivity of which is $\varepsilon_r = 4.50 + i0.019$ at a frequency of 2.4 GHz. Each analogue is a tetrahedral mesh-based wire frame where the relative filling density was chosen to approximately correspond to the supposed relative internal permittivities $\varepsilon_r = \varepsilon_r' + i\varepsilon_r''$ according to the process described in Saleh et al. (2021, 2021a). One of the analogues is a homogeneous model (HM) with a constant relative electric permittivity of $\varepsilon_r^{(i)} = 3.40 + i0.04$, while the other is a detailed model (DM) composed of a mantle covering an interior part and a deep interior void (Fig. 2). Motivated by findings suggesting the existence of a porous mantle (Jutzi & Benz 2017) and relatively low overall density (Carry 2012), allowing for the existence of macro-porosities such as voids, this three-layer structure was first introduced in the numerical study of Sorsa et al. (2019), in which tomographic reconstructions were found using a numerically simulated set of full-wave measurements. Later, the same structure was used as a basis for the manufacture of the analogue objects investigated in the present study, as described in detail in Sorsa et al. (2021a).

Table 1. Laboratory vs space radar analogy for a 0.205 m analogue in its largest dimension and the 535 m Itokawa asteroid in its largest dimension.

Analogue asteroid			Real asteroid	
FB [GHz]	Lab radar f_0	B/f_0	Space radar f_0	FB [MHz]
$f \in [2, 18]$	10 GHz	1.6	3.8 MHz	$f \in [0.76, 6.84]$
$f \in [3.5, 16]$	9.75 GHz	1.3	3.74 MHz	$f \in [1.31, 6.17]$
$f \in [3.5, 12]$	7.75 GHz	1.1	2.97 MHz	$f \in [1.34, 4.60]$

Notes. B/f_0 denotes the bandwidth (B) vs. centre frequency and FB the frequency band.

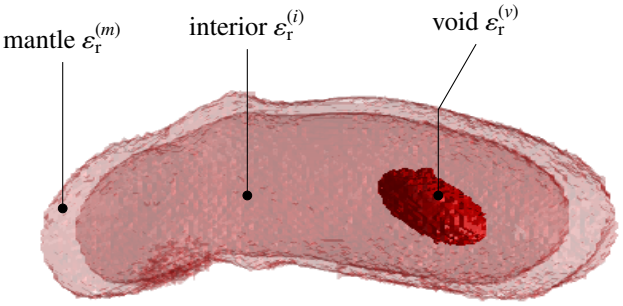

Fig. 2. 3D image of the DM analogue with the mantle layer and the deep interior void ($\varepsilon_r^{(m)} = 2.56 + i0.02$, $\varepsilon_r^{(i)} = 3.40 + i0.04$, $\varepsilon_r^{(v)} = 1$).

In the DM, the relative permittivity of the interior compartment coincides with that of the HM, while the mantle and void have lower values of $\varepsilon_r^{(m)} = 2.56 + i0.02$ and $\varepsilon_r^{(v)} = 1$. These relative permittivities were determined from measurements as described in a previous study (Eyraud et al. 2020). These two targets have already been employed in an analysis of signal propagation and back-propagation, comparing laboratory measurements for a single spatial point with calculated fields (Eyraud et al. 2020; Sorsa et al. 2021b). In the present study, we performed experiments using the frequency band from 2 to 18 GHz. The diameter of the bounding sphere is 0.24 m, which corresponds to 14.8 λ_m at the centre frequency f_0 considering the wavelength λ_m of the medium and 2.9 λ_m and 26.7 λ_m at the minimum and maximum frequency, respectively (Vaillon & Geffrin 2014). Given the real size of the Itokawa asteroid, our study corresponds to an equivalent experiment by microwave analogy of a space radar with a centre frequency of $f_0 = 3.74$ MHz and a bandwidth of $B = 4.86$ MHz. We note that the ratio bandwidth (B) versus centre frequency in our setup is larger than the one used for the CONSERT radar on board the Rosetta ESA mission ($B/f_0 = 0.1$) and the radar on board the Juventas cubesat in the HERA ESA mission ($B/f_0 = 0.3$). The laboratory-versus-space-radar analogy has been studied according to the different frequency bands investigated in this study and the results are shown in Table 1.

3. Laboratory measurements

The measurements of the two Itokawa analogues were made in a controlled environment, namely the anechoic chamber of the Centre Commun de Ressources en Microonde (CCRM) in Marseille, France (Geffrin et al. 2009). This chamber provides a spherical experimental setup, allowing measurements to be performed on a sphere encircling the target; here, in a quasi-monostatic configuration. For this purpose, the transmitting and

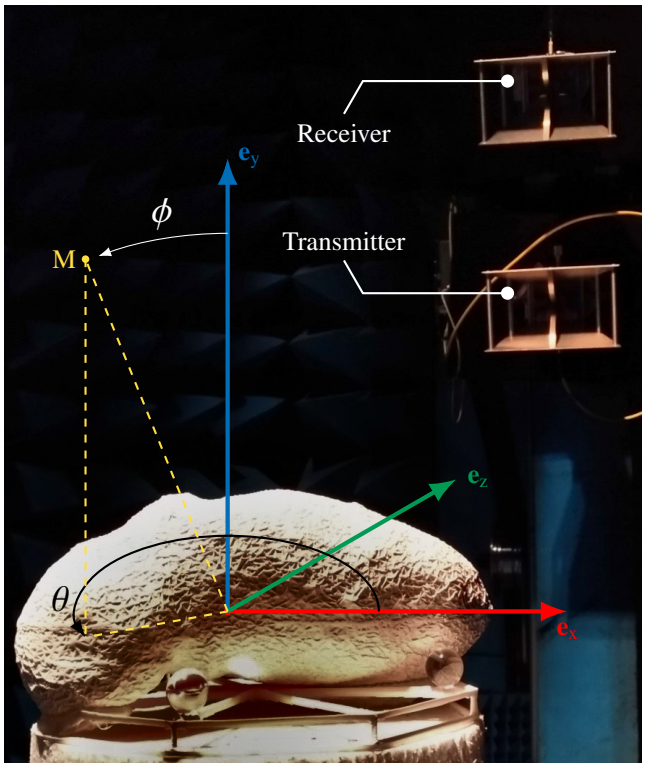

Fig. 3. Itokawa analogue in the anechoic chamber (the Plexiglas spheres, visible around the analogue, are here for alignment purposes and are removed during the measurements).

receiving antennas are spaced 12° apart in the elevation direction for all measurements (Fig. 3). The antennas are placed at a distance of $d = 1.794$ m from the centre of the analogues. The transmitting–receiving antenna pair can be moved by the elevation angle ϕ (ranging from −180° to 180°) and the target can be moved itself by the azimuthal angle θ (ranging from 26° to 154°; Fig. 3). The combination of movements allows us to explore almost the full sphere surrounding the target in the reference frame in which it is fixed. The angular step $\Delta\phi$ and $\Delta\theta$ are selected in concordance with the Nyquist sampling criterion, considering the maximum frequency (Bucci & Isernia 1997). To obtain a sampling step of 4° in all directions around the analogue, the angular sampling of the elevation angle is $\Delta\phi = 4°$. The azimuthal angular step is chosen according to the elevation angle: that is the azimuthal angular step is larger at the pole than in the horizontal plane, which results in an 'Igloo' configuration and alleviates the need to measure several points that might give the same information. This corresponds to a minimum pitch of $\Delta\theta = 4°$ at $\phi_s = 90°$ and a maximum pitch of $\Delta\theta = 9°$ at $\phi_s = 26°$. In addition, the 'Igloo' configuration allows

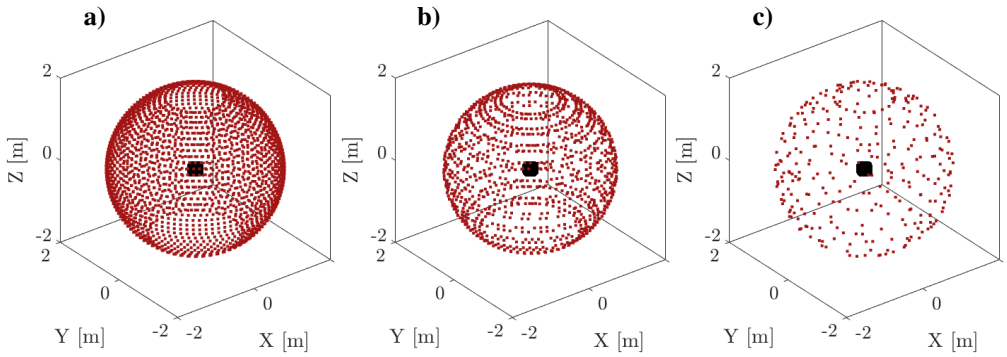

Fig. 4. Scheme of the measurement point distribution for different configurations. Panel a: all the measurements points. Panel b: selection of 1257 points. Panel c: selection of 363 points.

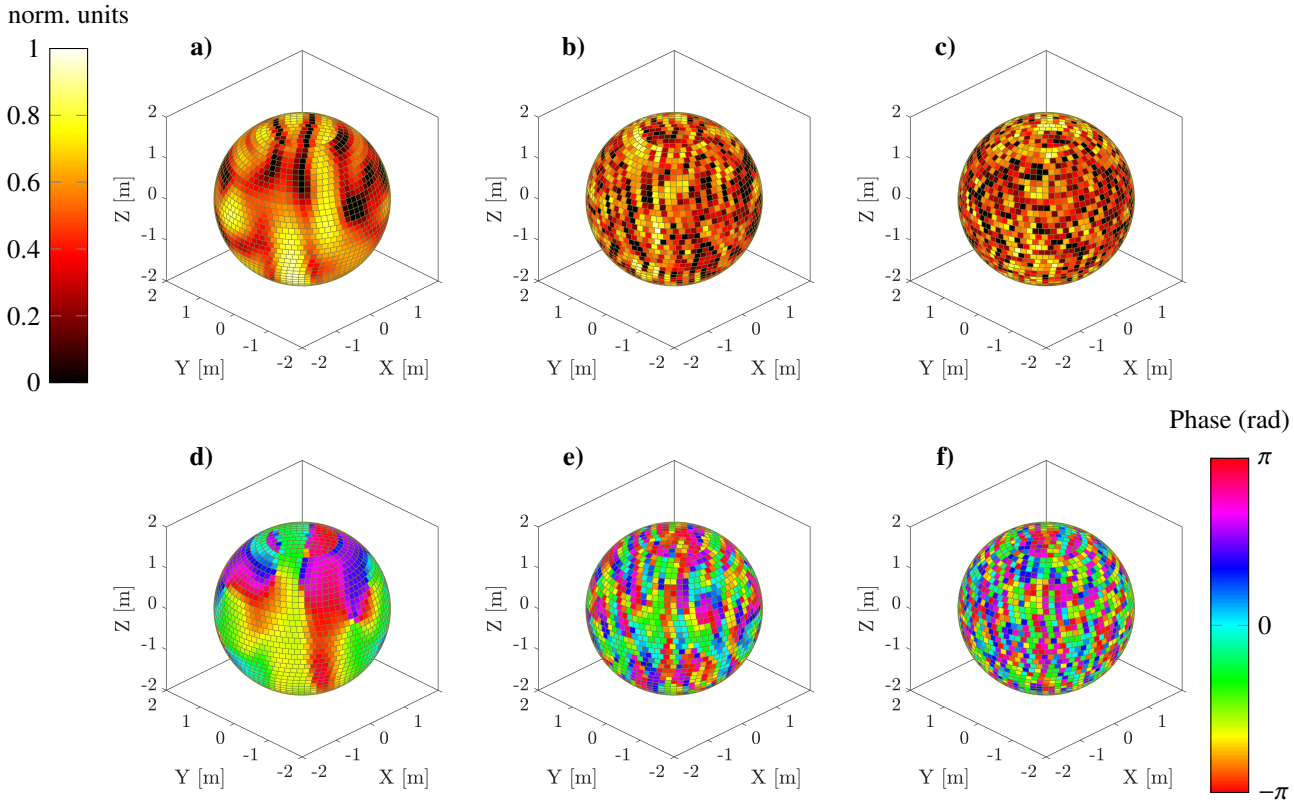

Fig. 5. Spatial variations of the modulus (a–c) and phase (d–f) of the scattered electric field measured in the anechoic chamber, at $f = 3.5$ GHz (left), $f = 10$ GHz (centre), and $f = 16$ GHz (right). These values of the scattered field are plotted on the positions corresponding to the configuration in Fig. 4a.

a reduction of the measurement time by around 30 % compared to regular angular spacing. The total number of spatial points (transmitter/receiver) is equal to $N = 2372$ as shown in Fig. 4a. The minimum, centre, and maximum frequencies are respectively $f_{\min} = 2$ GHz, $f_0 = 10$ GHz, and $f_{\max} = 18$ GHz, with a frequency step of $\Delta f = 0.05$ GHz, that is $N_f = 321$ frequencies. The polarisation is kept linear along the direction of the elevation unit vector for both the transmitter and the receiver.

The experimental scattered field is obtained by subtracting two fields: the first measured in the presence of the analogue and its pedestal, and the second with the pedestal only. This subtraction gives only the scattered field and reduces any pedestal effects. All these measurements are calibrated and post-processed with a reference target for which quantitative scattered fields can be extracted (Geffrin et al. 2009; Eyraud et al. 2008). Visualisations of the complex field are shown in Fig. 5. In this figure, the amplitude and phase of the scattered field are plotted at the angular positions corresponding to the configuration in Fig. 4a for different frequencies so that the evolution of the scattered electric field as a function of frequency is visible.

4. Inverse imaging procedure

4.1. Principle

Inverse imaging techniques are designed to obtain information about the scattering object based on the scattered field emanating from the target, which is illuminated with a known incident electromagnetic wave. The objective of inverse problems is

to determine the causes from the known effects (Bertero & Boccacci 1998). Here the effect is the measurement of the interaction of the incoming wave with the target, while the cause that is sought is the structure and position of the object. Finding a reconstruction necessitates solving an inverse problem, that is, an ill-posed problem without a unique solution, for which a given effect can follow from various different causes. However, in the case of the structural imaging implemented here, where the induced current is reconstructed (not the permittivity), the relationship between the desired physical quantity and the data is linear (see Eq. (1)), and a solution must exist, thus avoiding ill-posed problems, the effect of noise is also reduced.

In this study, the purpose is to obtain a fast structural visualisation of the object. Our imaging techniques are therefore based on the observation equation of the scattered field, which for a receiver placed at a position $\mathbf{r}_\Gamma$ can be written as

$$\mathbf{E}_{\text{sca}}(\mathbf{r}_\Gamma) = \iiint_\Omega \boldsymbol{\mathcal{G}}(\mathbf{r}_\Gamma, \mathbf{r}_\Omega)\mathbf{J}(\mathbf{r}_\Omega)\,\mathrm{d}\mathbf{r}_\Omega, \tag{1}$$

where $\boldsymbol{\mathcal{G}}$ is the dyadic free-space Green's function between the object zone Ω and the receiver zone Γ, and $\mathbf{J}$ is the induced current, written as

$$\mathbf{J}(\mathbf{r}_\Omega) = \chi(\mathbf{r}_\Omega)\mathbf{E}(\mathbf{r}_\Omega), \tag{2}$$

where $\chi(\mathbf{r}_\Omega) = k_0^2\varepsilon_{\text{r}}(\mathbf{r}_\Omega) - k_0^2$ is the permittivity contrast (k_0 being the wavenumber in vacuum) and $\mathbf{E}$ the electric field. This equation is used below to retrieve the induced currents, which allow both the external shape of the object and its internal structure to be visualised.

Considering the following far-field conditions:

$$\forall r_\Omega \in \Omega,\ k_0 r_\Gamma \gg 1,\ r_\Gamma \gg r_\Omega,\ \frac{k_0 r_\Omega^2}{2r_\Gamma} \ll 1, \forall r_\Gamma \in \Gamma, \tag{3}$$

with the time convention $-\mathrm{i}\omega t$, the dyadic free-space Green's function in spherical coordinates can be approximated as

$$\boldsymbol{\mathcal{G}}(\mathbf{r}_\Gamma, \mathbf{r}_\Omega) \approx \frac{\mathrm{e}^{\mathrm{i}\mathbf{k}_{\text{s}}\cdot(\mathbf{r}_\Gamma - \mathbf{r}_\Omega)}}{4\pi(\mathbf{r}_\Gamma - \mathbf{r}_\Omega)}\left[\mathbf{I} - \mathbf{e}_{r_\Gamma} \otimes \mathbf{e}_{r_\Gamma}\right], \tag{4}$$

where $\mathbf{k}_{\text{s}} = k_0\mathbf{e}_{r_\Gamma}$ depicts the scattered wave-vector, $\mathbf{I}$ is the identity operator, and $(\mathbf{e}_{r_\Gamma}, \mathbf{e}_{\theta_\Gamma}, \mathbf{e}_{\phi_\Gamma})$ is the vector basis of the spherical system of coordinates.

The Green's function depends on $\mathbf{k}_{\text{s}}$ and, by extension, on the relative permittivity of the propagation medium. If we consider that the wave propagation within the analogue takes place in a vacuum, this will lead to a reconstructed object with a distorted shape. The fact that the wave does not have the same velocity inside the object as outside is therefore taken into account in an approximate way. Based on an estimate of the permittivity of the medium, assumed homogeneous, inside the target, this value was determined from the far-field scattering pattern in the time domain for the central transmitter–receiver position ($\phi = 90°$ and $\theta = 174°$). The average permittivity can be approximated from the average wave velocity inside the target given the ratio between the diameter and the time difference between the two major peaks scattering from the two ends of the target (Eyraud et al. 2020). The time t taken for the wave to pass through the object is therefore easily calculated and the relative permittivity of the target is reached ($\varepsilon_{\text{r}} = 3.40$). In the calculation of the Green's function, this information is embedded in the scattered wave-vector:

$$\begin{cases} \mathbf{k}_{\text{s}} \cdot (\mathbf{r}_\Gamma - \mathbf{r}_\Omega) \approx \mathbf{k}_0 \cdot (\mathbf{r}_\Gamma - \sqrt{\varepsilon_{r_\Omega}}\mathbf{r}_\Omega), \\ \boldsymbol{\mathcal{G}}(\mathbf{r}_\Gamma, \mathbf{r}_\Omega) \approx \dfrac{\mathrm{e}^{\mathrm{i}(\mathbf{k}_0\cdot\mathbf{r}_\Gamma - \mathbf{k}_\Omega\cdot\mathbf{r}_\Omega)}}{4\pi(\mathbf{r}_\Gamma - \mathbf{r}_\Omega)}\left[\mathbf{I} - \mathbf{e}_{r_\Gamma} \otimes \mathbf{e}_{r_\Gamma}\right], \end{cases} \tag{5}$$

with $\mathbf{k}_0$ denoting the air wave-vector and $\mathbf{k}_\Omega$ the wave-vector that is defined in the domain Ω. In order to retrieve an estimate of the induced currents $\mathbf{J}$, that is, to provide a structural image of the analogues, the back-propagation and the pseudo-inverse reconstructions were evaluated.

4.1.1. Back-propagation

Back-propagation (BP) is one of the most commonly used methods (Bertero & Boccacci 1998) to obtain the induced currents. This technique provides an approximative solution of the induced currents using Eq. (1). For each frequency, an estimated value of the induced currents on the target zone ($\mathbf{r}_\Omega \in \Omega$), called $\mathbf{J}^{\text{BP}}$, is then obtained using all the receiving positions, as follows:

$$\mathbf{J}^{\text{BP}}(\mathbf{r}_\Omega, f) = \iiint_\Gamma \boldsymbol{\mathcal{G}}^\star(\mathbf{r}_\Omega, f, \mathbf{r}_\Gamma)\mathbf{E}_{\text{sca}}(\mathbf{r}_\Gamma)\mathrm{d}\mathbf{r}_\Gamma, \tag{6}$$

where $\boldsymbol{\mathcal{G}}^\star$ is the transpose-conjugate matrix of the dyadic Green's function $\boldsymbol{\mathcal{G}}$.

4.1.2. Pseudo-inverse method

The pseudo-inverse (PI) method is the least squares solution of the equation: $\widehat{\mathbf{J}} = \text{argmin}\{\|\mathbf{E}_{\text{sca}} - \mathbf{G}\mathbf{J}\|^2\}$. The PI method considers the pseudo-inverse matrix of the Green's function $\boldsymbol{\mathcal{G}}^+ = \boldsymbol{\mathcal{G}}^\star(\boldsymbol{\mathcal{G}}\boldsymbol{\mathcal{G}}^\star)^{-1}$ (Campbell & Meyer 2009). The results of the PI and BP methods are often very close as the only difference is that the BP method approximates $\boldsymbol{\mathcal{G}}\boldsymbol{\mathcal{G}}^\star$ as the identity matrix. The estimate of the induced currents retrieved in this case is as follows:

$$\mathbf{J}^{\text{PI}}(\mathbf{r}_\Omega, f) = \iiint_\Gamma \boldsymbol{\mathcal{G}}^+(\mathbf{r}_\Omega, f, \mathbf{r}_\Gamma)\mathbf{E}_{\text{sca}}(\mathbf{r}_\Gamma)\mathrm{d}\mathbf{r}_\Gamma. \tag{7}$$

4.2. Combination of the maps at different frequencies

Through the imaging procedure described above, we obtain 3D reconstructions of the induced currents over a band of N_f frequencies. With the assumption that ε_{r} (and therefore the contrast) does not change for the different frequencies, the reconstructed maps are summed over the frequencies (Catapano et al. 2008):

$$\mathbf{J}^i_\Gamma(\mathbf{r}_\Omega) = \sum_{k=1}^{N_{\text{f}}} \mathbf{J}^i(\mathbf{r}_\Omega, f_k),\ i = \{\text{BP}, \text{PI}\}\ . \tag{8}$$

4.3. Implementation

The induced current maps are reconstructed in the domain Ω containing the analogue, and so the domain must be carefully chosen. This domain is larger than the analogue dimensions, and can be described as a $0.4 \times 0.4 \times 0.4\,\text{m}^3$ cube containing a three-dimensional grid of points placed inside. This cube corresponds to a side length of $44.4\lambda_{\text{m}}$ and $4.9\lambda_{\text{m}}$ with respect to the maximum and minimum signal frequency f_{max} and f_{min},

with λ_m denoting the corresponding wavelength inside the analogue. The grid step is defined as $\Delta l = \lambda_{f_{max}}/3 \approx 5.6$ mm for each frequency, which can be considered appropriate regarding both spatial resolution and computational cost.

In addition, the scattered field obtained from the measurement points must be interpolated so as to obtain field values on uniformly distributed reception points. As explained in Sect. 3, an 'Igloo' configuration is used, which does not have a uniform angular step, that is, the scattered field obtained from the measurements has to be interpolated before it can be inverted, as the algorithm used requires a regular step for both angles. The scattered field is interpolated on a sphere with a method based on linear Delaunay triangulation (de Berg et al. 2008).

5. Optimisation of the number of measurement points

5.1. Reduction of the frequencies number

Radar systems often provide wide frequency bands in order to process the signals in the time domain. Working in the time domain for imaging is an interesting way to see the interfaces between media of different permittivities using the temporal echo produced by the reflection of the wave at that interface. In the procedures that use frequency domain, the refocusing of the field on the inhomogeneities first exploits the spatial information diversity (then possibly the frequency diversity in a second step). This type of imaging procedure is not affected by the dispersive mechanism (in which permittivity varies with frequency). Moreover, working in the frequency domain makes it easier to reduce the number of useful frequencies. In this study, we will see that we do not necessarily need all the frequencies. In order to optimise the computation procedure, we carried out two experiments to investigate the dependency of our procedure on the frequencies used. The first is designed to distinguish whether or not it is possible to obtain correct reconstructions by reducing the frequency band. The second experiment looks at the effects of an increase in the frequency step to reduce the number of frequencies while maintaining the same frequency band.

5.1.1. Frequency band

It is important to note that the mesh pitch of our analogues is 4 mm, which is greater than $\lambda_m/3$ for frequencies above 16 GHz (Saleh et al. 2021). The mesh size is therefore not sufficient to consider the analogue as a homogeneous medium (or piecewise homogeneous for the DM analogue) for such frequencies and the mesh effect will be visible. Therefore, frequencies above 16 GHz are omitted. In the low part of the frequency band, the antenna coupling between the transmitter and the receiver is predominant, and so we choose not to use these frequencies for the inversion process and start at 3.5 GHz. This study is based on the idea that most of the energy of the scattered field is in the low frequencies, that is, the information contained in the high frequencies is not likely to improve the reconstructions. It could even lead to the deterioration of the reconstructions (see Sect. 6.3). As the whole frequency band (from 3.5 to 16 GHz) might not be entirely useful for finding a reconstruction, a reduction of the frequency band is investigated. The maximum frequency of interest, that is, the maximum frequency above which the following frequencies will not be considered, can be quantified by studying the energy profile of the scattered field as a function of frequencies

$$W(f) = \frac{\sum_{r_\Gamma} |E_{sca}(\mathbf{r}_\Gamma, f)|^2}{\sum_f \sum_{r_\Gamma} |E_{sca}(\mathbf{r}_\Gamma, f)|^2}. \quad (9)$$

We have chosen to keep only the frequencies from 3.5 to 12 GHz, which corresponds to 74.7% of the total energy (considering the 3.5–16 GHz band) and a bandwidth versus centre frequency ratio of $B/f_0 = 1.1$. We note that considering the whole frequency band leads to $B/f_0 = 1.3$.

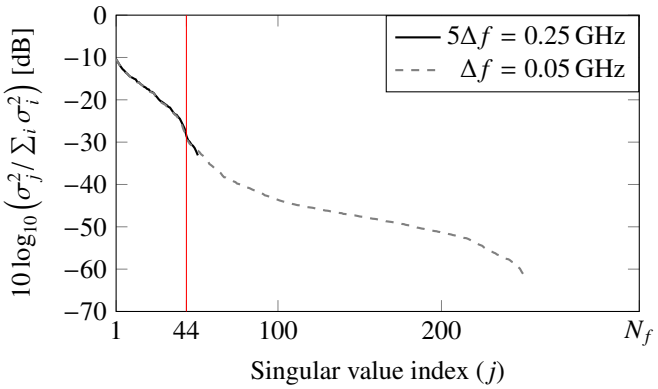

Fig. 6. Singular values of the scattered field: σ, for two different frequency steps. In both cases, the data are normalised according to the sum of the squared singular values of each case. The vertical red line corresponds to the cut-off obtained from the derivative of the curve.

5.1.2. Number of frequencies

As explained above, in order to analyse the signal in the time domain, the frequency step of the measurement has to be sufficiently small. However, in the frequency domain, such a step is potentially unnecessary. In this part, we therefore examine the effects of increasing the frequency step. In order to find the suitable step size, we performed a singular value decomposition (SVD; Wendland 2018) of the scattered field matrix depending on the receiver positions $\mathbf{r}_\Gamma$ and on the frequencies:

$$\mathbf{E}_{sca}(\mathbf{r}_\Gamma, f) = \mathbf{U}\mathbf{\Sigma}\mathbf{V}^\dagger. \quad (10)$$

The $\mathbf{\Sigma}$ matrix contains the singular values σ_i sorted by their impact in the scattered field matrix. SVD allows us to identify the approximate number of useful frequencies contributing to the space of informative signals and the number of frequencies constituting the noise space. We note that the spatial sampling is chosen according to the Nyquist sampling criterion (Bucci & Isernia 1997), and so the cut-off on the spectrum corresponds to the frequency and not to the angular positions. In order to find this number, the diagonal entries of $\mathbf{\Sigma}$ (corresponding to the singular values σ_i) are plotted in Fig. 6 and its derivative is calculated giving the cut-off of the spectrum at 44 frequencies, meaning that 44 frequencies contain a suitable amount of information on the scattered field a priori. We chose to select this number of frequencies in an evenly spaced manner, giving a frequency step of 0.25 GHz or $5\Delta f$. The choice is supported by the plot of the spectrum of singular values of the reduced scattered field strength considering the 3.5–16 GHz band with a step of $5\Delta f$, which is close to the step used with the full frequency band.

5.2. Reduction of the number of measurement positions

The frequency band reduction implies a reduction in the number of measurement points. Considering that the measurements are performed on a sphere enclosing the target, the minimal elevation and azimuthal angular step (respectively $\Delta\phi$ and $\Delta\theta$) are calculated according to Bucci & Isernia (1997), as

$$\Delta\theta = \Delta\phi = \frac{c}{2 f_{\mathrm{M}} a}, \tag{11}$$

where a is the radius of the smallest sphere that can contain the object, c is the velocity of light in vacuum, and f_{M} is the maximum frequency. A band from 3.5 to 12 GHz with a frequency step of Δf leads to an angular step of 6° for both angles θ and ϕ, leading to 1257 points evenly distributed on a sphere surrounding the object, as shown in Fig. 4b.

5.3. Spatial configuration selection

This section concentrates on the effects of a large angular step on the reconstructions, a step that would be much larger than that recommended by Eq. (11) and therefore by Bucci & Isernia (1997). This study is motivated by the results obtained in Sorsa et al. (2023). A configuration of a sparse point selection of the transmitter is therefore used, selecting 363 from the 2372 measurement points. This configuration corresponds to an angular step of 20° as shown in Fig. 4c. The angular step is chosen so that the points are evenly distributed as described in Paper II (Sorsa et al. 2023).

6. Imaging results

The reconstructed maps are structural, that is, they provide information on the position and shape of the heterogeneities, but not on the permittivity values. Therefore, we choose to normalise the maps between 0 and 1:

$$\mathbf{J}^i_{\mathrm{f,n}} = \frac{|\mathbf{J}^i_{\mathrm{f}}| - \min\left(|\mathbf{J}^i_{\mathrm{f}}|\right)}{\max\left(|\mathbf{J}^i_{\mathrm{f}}|\right) - \min\left(|\mathbf{J}^i_{\mathrm{f}}|\right)}. \tag{12}$$

6.1. Quantitative quality measures

In order to obtain a quantitative estimation of the imaging results, we set up quantitative quality measures for comparing the maps. Each 3D reconstructed normalised map $\mathbf{J}^{i,\mathrm{r}}_{\mathrm{f,n}}$ is compared with the real 3D-normalised map $\mathbf{J}^{i,\mathrm{t}}_{\mathrm{f,n}}$ using different quantitative quality measures. We consider the following quantitative quality measures: root mean square error (RMSE), correlation (C), and relative overlap (RO).

The first quantitative quality measure, RMSE, is a classical and widely used quantitative quality measure for comparing images:

$$\begin{aligned}
\mathrm{RMSE}^{\alpha} &= \sqrt{\frac{1}{N^{\alpha}_{\Omega}} \sum_k \mathrm{M}^{\alpha}\left(\mathbf{J}^{i,\mathrm{t}}_{\mathrm{f,n}}\left(\mathbf{r}^k_{\Omega}\right) - \mathbf{J}^{i,\mathrm{r}}_{\mathrm{f,n}}\left(\mathbf{r}^k_{\Omega}\right)\right)^2}, \\
\mathrm{M}^{\alpha} &= \begin{cases} 1 & \forall k \in \alpha \\ 0 & \text{otherwise,} \end{cases} \\
\alpha &= \text{void, ext or all,}
\end{aligned} \tag{13}$$

with N_{Ω} and N^{α}_{Ω} denoting the total and α number of cells, respectively. The RMSE quantitative quality measure was applied to particular areas of the map: the entire map $\mathrm{RMSE}^{\mathrm{all}}$, the outer area, that is, outside the analogue $\mathrm{RMSE}^{\mathrm{ext}}$, and the void area $\mathrm{RMSE}^{\mathrm{void}}$ (for DM only). The mask M varies according to the selected area. For example, in the case of $\mathrm{RMSE}^{\mathrm{ext}}$, M is a 3D matrix of the same size as the maps, equal to 1 in the outer area of the analogue and 0 elsewhere. We note that for $\mathrm{RMSE}^{\mathrm{void}}$, in our reconstructions the void radiates in high values due to the fact that it is a map of induced current (and not of contrast), and so the theoretical values are changed to ones instead of zeroes.

We also consider the linear correlation between the two maps:

$$\begin{aligned}
C^{\alpha} &= 100 \left| \frac{\mathrm{Cov}^{\mathrm{M}}\left(\mathbf{J}^{i,\mathrm{r}}_{\mathrm{f,n}}, \mathbf{J}^{i,\mathrm{t}}_{\mathrm{f,n}}\right)}{\sqrt{\mathrm{Var}^{\mathrm{M}}\left(\mathbf{J}^{i,\mathrm{r}}_{\mathrm{f,n}}\right) \mathrm{Var}^{\mathrm{M}}\left(\mathbf{J}^{i,\mathrm{t}}_{\mathrm{f,n}}\right)}} \right| \\
&= 100 \left| \frac{\sum_k \mathrm{M}^{\alpha}\left(\mathbf{J}^{i,\mathrm{t}}_{\mathrm{f,n}}\left(\mathbf{r}^k_{\Omega}\right) - \overline{\mathbf{J}^{i,\mathrm{t}}_{\mathrm{f,n}}\left(\mathbf{r}^k_{\Omega}\right)}\right)\left(\mathbf{J}^{i,\mathrm{r}}_{\mathrm{f,n}}\left(\mathbf{r}^k_{\Omega}\right) - \overline{\mathbf{J}^{i,\mathrm{r}}_{\mathrm{f,n}}\left(\mathbf{r}^k_{\Omega}\right)}\right)}{\sqrt{\mathrm{Var}^{\mathrm{M}}\left(\mathbf{J}^{i,\mathrm{r}}_{\mathrm{f,n}}\left(\mathbf{r}^k_{\Omega}\right)\right) \mathrm{Var}^{\mathrm{M}}\left(\mathbf{J}^{i,\mathrm{t}}_{\mathrm{f,n}}\left(\mathbf{r}^k_{\Omega}\right)\right)}} \right|, \\
\mathrm{M}^{\alpha} &= \begin{cases} 1 & \forall k \in \alpha \\ 0 & \text{otherwise,} \end{cases} \\
\alpha &= \text{int, ext or all,}
\end{aligned} \tag{14}$$

with the variance $\mathrm{Var}^{\mathrm{M}}\left(\mathbf{J}^i_{\mathrm{f,n}}\left(\mathbf{r}^k_{\Omega}\right)\right) = \sum_k \mathrm{M}^{\alpha}\left(\mathbf{J}^i_{\mathrm{f,n}}\left(\mathbf{r}^k_{\Omega}\right) - \overline{\mathbf{J}^i_{\mathrm{f,n}}\left(\mathbf{r}^k_{\Omega}\right)}\right)^2$, $\mathrm{Cov}(\bullet, \bullet)$ denoting the covariance operator, and $\overline{\mathbf{J}^i_{\mathrm{f,n}}\left(\mathbf{r}^k_{\Omega}\right)}$ the mean of the values of $\mathbf{J}^i_{\mathrm{f,n}}\left(\mathbf{r}^k_{\Omega}\right)$. To separately evaluate the different areas of the map, we calculated three correlations: on the entire map C^{all}, on the outer area C^{ext} (only the domain outside the analogue is considered), and on the interior part of the analogue C^{int} (only the domain inside the analogue is considered). The RO (Sorsa et al. 2020, 2023) is defined as

$$\mathrm{RO} = 100\left(\frac{\mathrm{Area}(\mathcal{A})}{\mathrm{Area}(S)}\right), \tag{15}$$

where $\mathcal{A} = S \cap \mathcal{R}$ is the overlap between the set S to be recovered, that is, the theoretical map, and the set $\mathcal{R}$, the reconstructed map, in which a given reconstruction is greater than a limit, such that $\mathrm{Area}(\mathcal{R}) = \mathrm{Area}(S)$. This quantitative quality measure is only used for the overlap between the reconstructed map and the theoretical map of the void for the DM analogue. Considering the theoretical void area divided into n_v voxels, RO evaluates the percentage of these voxels reconstructed inside the map. We note that the more similar the two maps are, the closer the RMSEs are to zero, and the closer the correlations and RO are to 100%. The correlations and RO values are presented as percentages.

6.2. Algorithm influence

In Sects. 4.1.1 and 4.1.2, we describe the two imaging methods that were implemented, namely the BP and PI techniques. In this section, the BP and PI reconstructions are presented and compared. For these reconstructions, the entire frequency range from

Table 2. Overview of the quantitative quality measures of HM reconstructions.

Row	Method	FB [GHz]	# points	$\mathrm{RMSE}^{\mathrm{all}}$	$\mathrm{RMSE}^{\mathrm{ext}}$	$\mathrm{RMSE}^{\mathrm{void}}$	$C^{\mathrm{all}}(\%)$	$C^{\mathrm{int}}(\%)$	$C^{\mathrm{ext}}(\%)$	RO(%)
1	BP	$f \in [3.5, \Delta f, 16]$	2372	0.143	0.110	–	18.8	63.6	2.6	–
2	PI	$f \in [3.5, \Delta f, 16]$	2372	0.143	0.110	–	18.8	63.7	2.6	–
3	PI	$f \in [3.5, \Delta f, 12]$	2372	0.150	0.122	–	21.0	69.6	2.9	–
4	PI	$f \in [12, \Delta f, 16]$	2372	0.168	0.146	–	21.5	69.9	2.8	–
5	PI	$f \in [3.5, 5\Delta f, 16]$	2372	0.147	0.116	–	19.9	65.8	2.8	–
6	PI	$f \in [3.5, 5\Delta f, 12]$	2372	0.151	0.125	–	22.1	71.2	3.0	–
7	PI	$f \in [3.5, 5\Delta f, 12]$	1257	0.155	0.130	–	22.6	72.5	3.1	–
8	PI	$f \in [3.5, 5\Delta f, 12]$	363	0.134	0.093	–	16.9	59.6	2.2	–

Table 3. Overview of the quantitative quality measures of DM reconstructions.

Row	Method	FB [GHz]	# points	$\mathrm{RMSE}^{\mathrm{all}}$	$\mathrm{RMSE}^{\mathrm{ext}}$	$\mathrm{RMSE}^{\mathrm{void}}$	$C^{\mathrm{all}}(\%)$	$C^{\mathrm{int}}(\%)$	$C^{\mathrm{ext}}(\%)$	RO(%)
1	BP	$f \in [3.5, \Delta f, 16]$	2372	0.113	0.079	0.763	23.7	69.0	3.3	19.1
2	PI	$f \in [3.5, \Delta f, 16]$	2372	0.113	0.079	0.763	23.7	69.1	3.3	19.1
3	PI	$f \in [3.5, \Delta f, 12]$	2372	0.116	0.086	0.721	24.7	71.1	3.4	25.4
4	PI	$f \in [12, \Delta f, 16]$	2372	0.151	0.134	0.722	21.9	71.1	2.9	5.8
5	PI	$f \in [3.5, 5\Delta f, 16]$	2372	0.115	0.083	0.755	23.8	68.9	3.3	20.6
6	PI	$f \in [3.5, 5\Delta f, 12]$	2372	0.118	0.089	0.718	25.0	70.6	3.4	25.4
7	PI	$f \in [3.5, 5\Delta f, 12]$	1257	0.118	0.089	0.707	25.2	70.9	3.4	27.0
8	PI	$f \in [3.5, 5\Delta f, 12]$	363	0.116	0.080	0.837	18.0	64.1	2.2	1.6

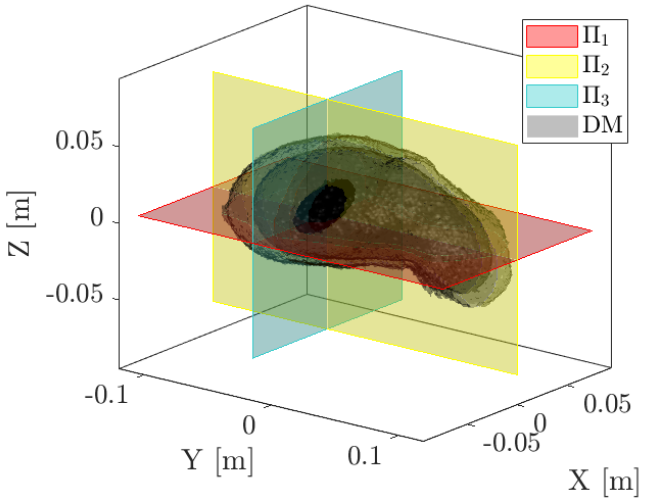

Fig. 7. Visualisation of the three planes on the theoretical 3D map (see Fig. 2), which coincide with the 2D slices of the reconstructions.

3.5 to 16 GHz and all transmitter–receiver pairs are used. Figures 8 and A.1, for the PI and BP methods respectively, the 2D slices of the 3D qualitative map obtained for the amplitude of the induced currents (as defined in Eqs. (6)–(8)). The location and orientation of these slices are shown in Fig. 7. Three planes have been specifically chosen so that each plane passes through the centre of the void. For Π_1 and Π_2, the planes correspond to $Z = 0\,\mathrm{mm}$ and $Y = 0\,\mathrm{mm}$, but the plane Π_3 is passing through $X = -33.4\,\mathrm{mm}$. In both cases, the external shape of the two analogues is reconstructed with an appropriate volume size. For both methods, a brighter area is highlighted on the DM reconstructions that corresponds to the deep-lying void. The reconstruction of the void is obtained at a position slightly out of line with where it should be, as one can observe from the white line corresponding to the theoretical contour. Some disturbances are also visible outside and inside the analogue. We discuss these points in the following sections. Comparing Figs. 8 and A.1 visually, it can be observed that the reconstructions obtained using the PI and BP methods do not show major differences.

In order to carry out a more rigorous comparison, the quantitative quality measures presented in Sect. 6.1 are evaluated and grouped in the first two rows of Tables 2 and 3. The correlation values remain far from what they should be in a perfect reconstruction, except for C^{int}. However, these quantitative quality measures are especially useful for comparing the different reconstructions with each other. We notice that the interior of the analogue is the area with the greatest influence on the C^{all} quantitative quality measure. The outer area of the analogue, which has a value of close to zero, contributes only slightly to this quantitative quality measure.

Previously we noticed that the inner part of the analogue reconstruction was not homogeneous and showed disturbances. This can be expected to follow from the fact that, in our inversion procedure, we do not account for the multiple scattering. This point is developed further later in this article. Although the overlap value is closer to 0 than to 100, it indicates a good quality void reconstruction (Sorsa et al. 2023). We notice a deviation of the void reconstruction in comparison with the theoretical one of about two or three voxels in Y and Z: $\Delta Y = \Delta Z \approx 10{-}15\,\mathrm{mm}$ and no deviation in X. This slight deviation roughly corresponds to the resolution limit $\lambda_{\mathrm{m}}/2$ of these reconstructions: that is, the maximum expected resolution is 8.35 mm at the centre frequency (9.75 GHz).

When comparing the quantitative quality measures between the two methods, no significant differences were found. Based on the quantitative quality measures, we conclude that BP and PI methods offer the same quality of reconstruction. For the rest of the study, we therefore use PI, which is the more methodologically advanced of the two.

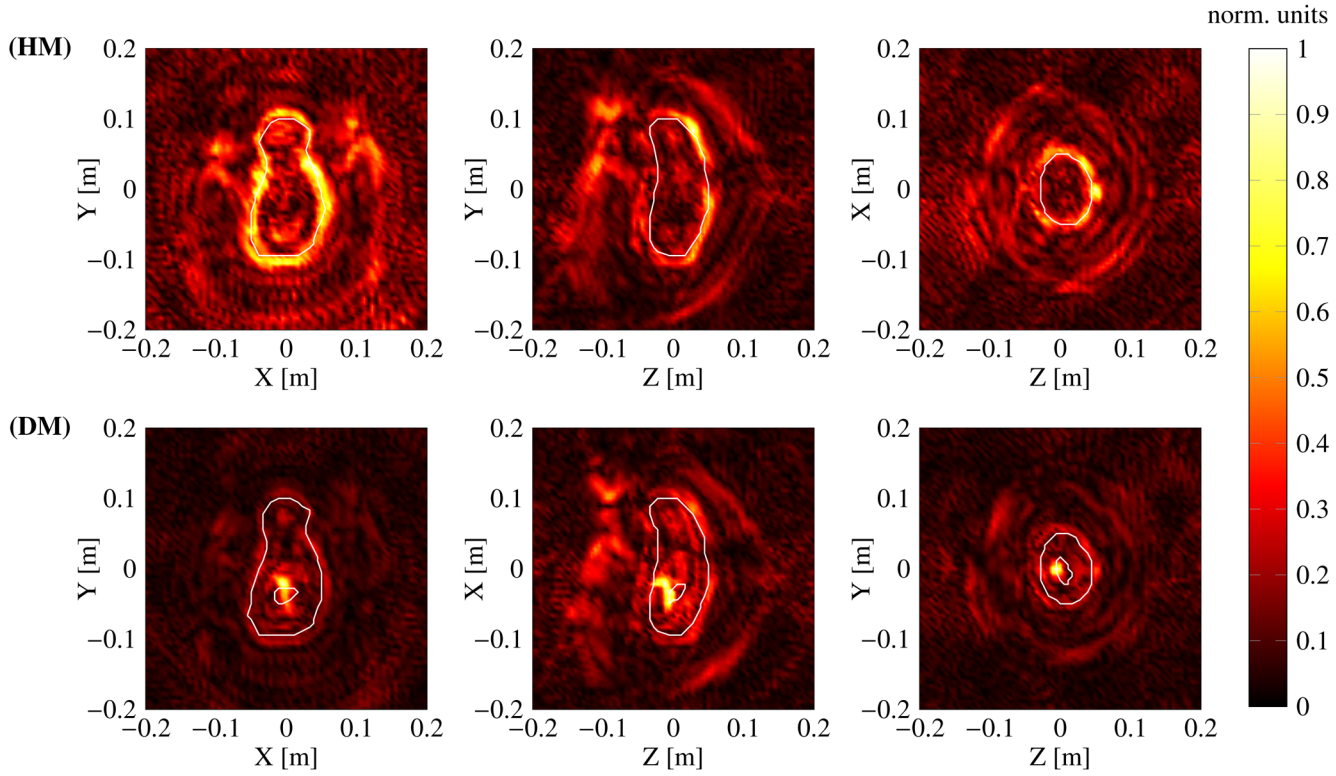

Fig. 8. Slices of the amplitude of the reconstructed induced currents using the PI method for both analogues from measured scattered field considering the 3.5–16 GHz frequency range and a frequency step of Δf. The line plot corresponds to the theoretical analogue. The figures on the left correspond to the plane Π_1, those in the middle to the plane Π_2, and those on the right to the plane Π_3.

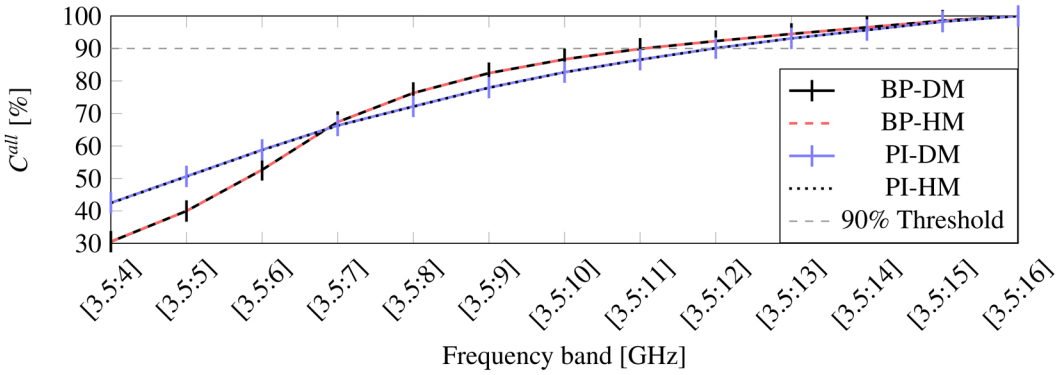

Fig. 9. Correlation coefficient between the reconstructions with the full frequency band 3.5–16 GHz with a frequency step of Δf and those taking into account a different frequency band for the BP-HM, BP-DM, PI-HM, and PI-DM cases. The horizontal grey dashed line corresponds to the 90% threshold for C^{all}.

6.3. Frequency band influence

In Sect. 5.1.1, we looked at the possibility of reducing the frequency band from 3.5–16 GHz to 3.5–12 GHz by examining the scattered field matrix. To support this choice, reconstructions taking into account the whole frequency band (from 3.5 to 16 GHz with a frequency step of Δf) are compared with those with the reduced frequency band and the correlation coefficients C^{all} between these reconstructions are calculated. We note that the coefficients are calculated on a cube including the object smaller than the domain Ω. Therefore, the C^{all} values for the HM and DM model reconstructions are presented in Fig. 9 for both methods. We chose to consider that the reconstructions are sufficiently accurate when the correlation coefficient is close to 90%. This level is reached for all configurations with the 3.5-12 GHz band. However, in both cases, the coefficient C^{all} increases significantly when the low frequencies are taken into account, that is, C^{all} increases by about 60 and 40 percentage points from the 3.5–4 band to the 3.5–12 GHz band for the HM and DM model, respectively, whereas it only increases by about 10 percentage points from the 3.5–12 to the 3.5–16 GHz band. This confirms our choice to reduce the frequency band from 3.5–16 to 3.5–12 GHz and, more generally, confirms that the low frequencies are predominant in our reconstructions.

The frequency range is therefore reduced from 3.5–16 to 3.5–12 GHz, while the rest of the algorithm remains unchanged and the frequencies taken into consideration are always summed together. The reconstructions are shown in Fig. 10 and in this situation $B/f_0 = 1.1$. The external shape and deep interior void remain visible. Here, an important aspect is that the artefacts

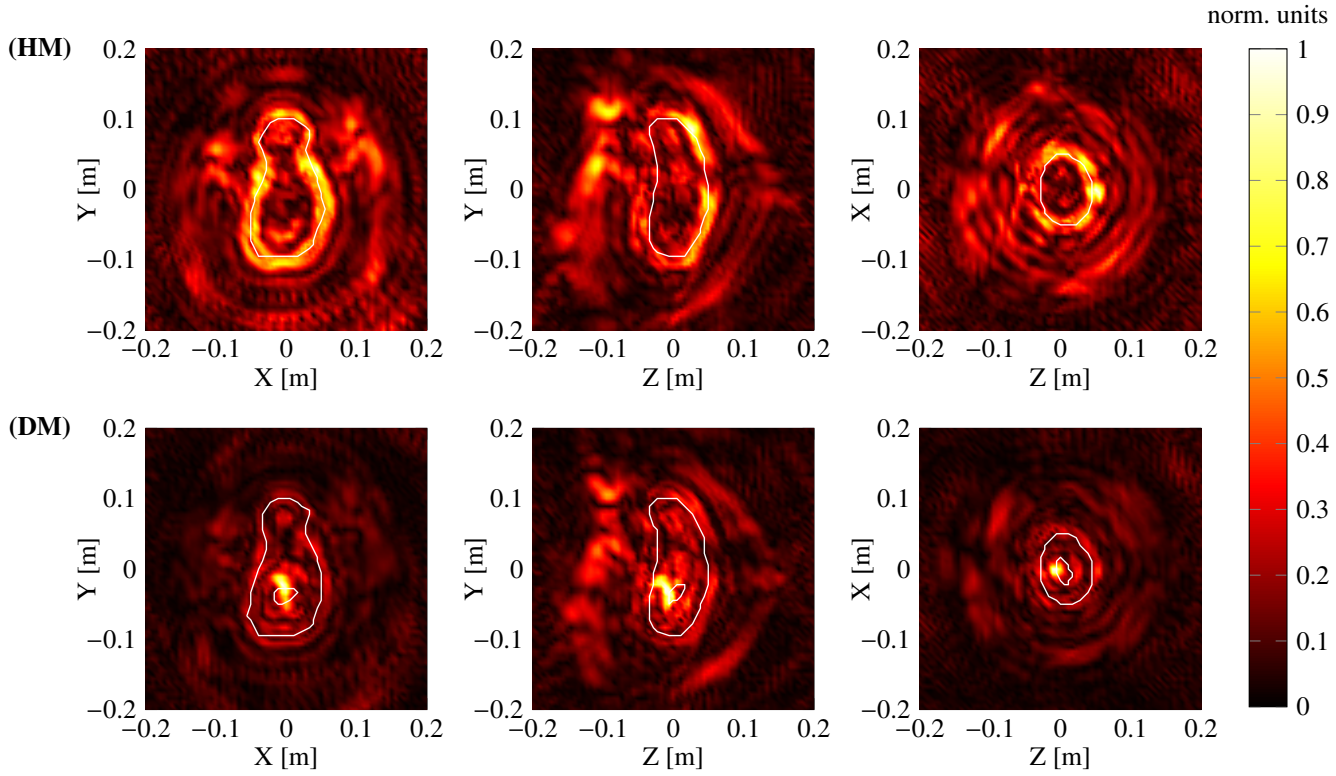

Fig. 10. Slices of the amplitude of the reconstructed induced currents using the PI method for both analogues considering the 3.5–12 GHz band and a frequency step of Δf. The line plot corresponds to the theoretical analogue. The figures on the left correspond to the plane Π_1, those in the middle to the plane Π_2, and those on the right to the plane Π_3.

surrounding the object (fast spatial variations) are largely reduced, providing a smoother representation compared to that obtained by considering the whole frequency band as depicted in Fig. 8. The location of the deep interior void seems to be unchanged from its location on the theoretical map and also from the full band reconstructions.

The quantitative quality measures presented in Sect. 6.1 are calculated and grouped on the third row of Tables 2 and 3 and they are to be compared with the quantitative quality measures obtained for the PI method provided in the second row of the tables. The quantitative quality measures C^{ext}, RMSE^{all}, and RMSE^{ext} are very close to the previously obtained values, with no significant differences. In addition, quantitative quality measures C^{all} and C^{int} are enhanced by 1–2% in the case of the reduced frequency band for the DM and 2–6% for the HM. Similarly, the void reconstruction is also of better quality according to the RO and $\text{RMSE}^{\text{void}}$.

The improvement of the quality measures can be explained by the fact that we reconstruct the induced current $\mathbf{J} = \chi\mathbf{E}$ (see Eqs. (6) and (7)) and not the contrast term χ. The field $\mathbf{E}$ is the sum of the incident field and the multiple scattering term $(\mathbf{E}(\mathbf{r}_\Gamma) = \mathbf{E}_i(\mathbf{r}_\Gamma) + \iiint_\Omega \mathcal{G}(\mathbf{r}_\Gamma, \mathbf{r}_\Omega)\mathbf{J}(\mathbf{r}_\Omega)\,\mathrm{d}\mathbf{r}_\Omega)$, which cannot be neglected in our case. In other words, $\mathbf{E}$ cannot be approximated by the incident field (Born approximation), especially for high frequencies. This field has potentially rapid spatial variations within the domain Ω, especially in high frequencies, with very localised areas where the field amplitude is strong (see e.g. Fig. 2 in Sorsa et al. 2021b). This results in reconstructions that are not easily interpreted without further non-linear processing. By removing high frequencies, this problem is mainly avoided, because we only consider frequencies for which the field inside the target is not spatially disturbed and for which it is possible to obtain contrast information from the induced currents map. However, the elimination of high frequencies reduces the potential spatial resolution of our reconstructions, which may cause an important loss of information about the void. To verify this, reconstructions considering the high frequencies (12–16 GHz band with a frequency step of Δf) of the initial frequency band are evaluated. In this situation $B/f_0 = 0.3$. The results are shown in Fig. A.2, where it is no longer possible to see the information on the external shape of the target. It might be possible to distinguish the void, but not easily. It should be noted that it would be possible to perform image processing on these reconstructions. However, here we choose to present the raw results to facilitate image comparisons and to improve our understanding of the evolution of the quantitative quality measures. In addition, the difference of the maps presented in Figs. 8 and 10 has been evaluated and is shown in Fig. A.5. In terms of HM reconstruction, some differences between the two maps are visible in the inner part of the surface; as to DM reconstructions, some higher intensity values are distinguishable near the interior void area. Therefore, some information has been lost. Nevertheless, the maximum intensity difference does not exceed 0.2, meaning that the loss of information is insignificant.

6.4. Frequency step influence

The aim of this section is to optimise the inversion procedure, particularly by looking at a reduction in the number of useful frequencies. In Sect. 5.1.2, we studied the SVD of the scattered field matrix. In particular, it was justified that selecting only 44 isotropically distributed frequencies should have the same information content as the 250 total frequencies. It should be

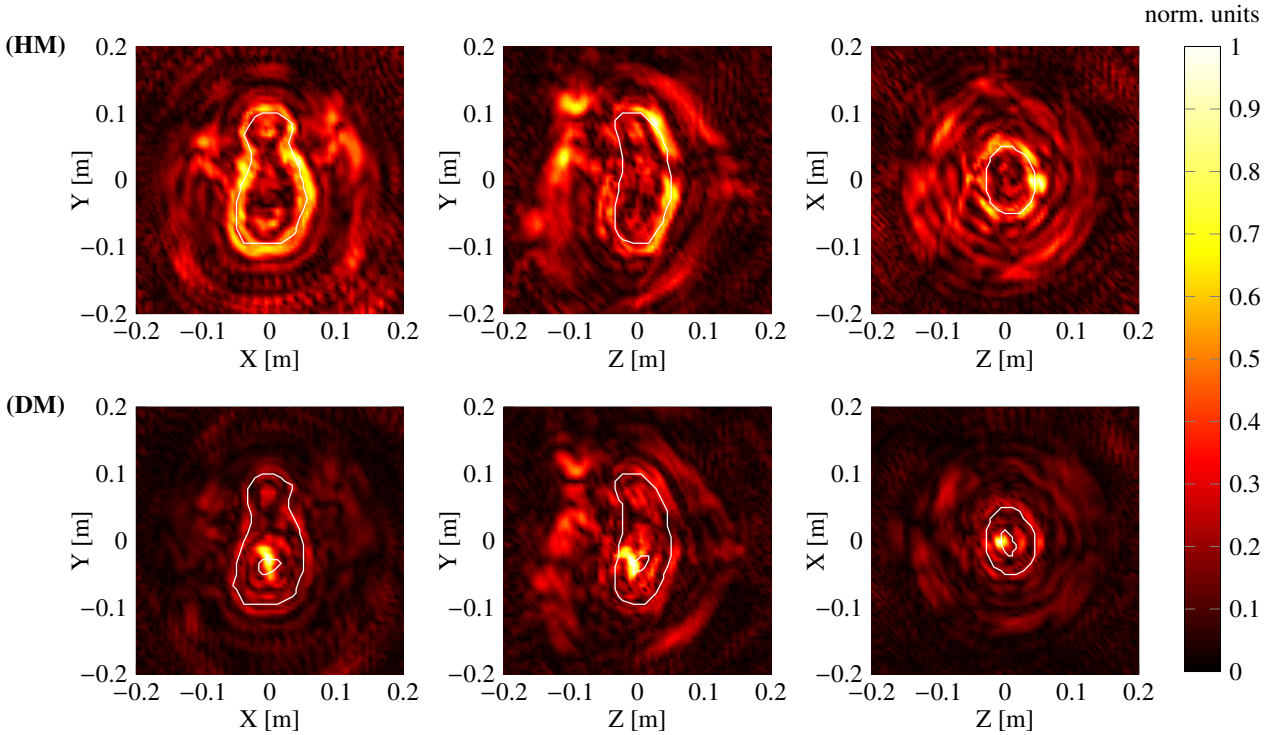

Fig. 11. Slices of the amplitude of the reconstructed induced currents using the PI method for both analogues with 35 frequencies considering the 3.5–12 GHz range with a step of $5\Delta f$. The line plot corresponds to the theoretical analogue. The figures on the left correspond to the plane Π_1, those in the middle to the plane Π_2, and those on the right to the plane Π_3.

noted here that it was not possible to select exactly 44 frequencies isotropically distributed from the 250 as the new frequency step must be in agreement with the measured one. Therefore, 51 frequencies were selected in the reconstructions presented in this section. The reconstructions taking into account a frequency band from 3.5 to 16 GHz with a frequency step of $5\Delta f$ are shown in Fig. A.3. Comparing these with the reconstruction obtained by considering the whole frequency band in Fig. 8, we do not notice any major differences. Both the external shape and the void are reconstructed with the same quality and the visible disturbances around the object do not seem to be reduced.

In order to compare these reconstructions more accurately, the quantitative quality measures are evaluated and presented in the fifth row of Tables 2 and 3. These are to be compared with those obtained for the reconstructions considering the 3.5–16 GHz band with a frequency step of Δf and the PI method presented in the second row of the same tables. For all quantitative quality measures of the HM and DM reconstructions, the values are in good agreement and the differences are not significant. In conclusion, the quantitative quality measures show that the reconstructions with 51 frequencies are similar to those with 250 frequencies. This was expected, because we have chosen these frequencies to have the same information content (see Sect. 5.1.2). It should also be noted that the choice to select these frequencies as isotropically distributed is justified here by the similarity of the reconstructed maps in the two situations. Below, we therefore consider this new frequency step as well as the reduced frequency band.

6.5. Influence of the new frequency step and reduction of the frequency band

In Sects. 6.3 and 6.4, we show that it is possible to reduce the frequency band and to increase the frequency step without losing reconstruction quality and even to improve the image with the reduction of the frequency band. Here, we combine these two parameters of the setup and analyse the effects on the reconstructions. Figure 11 shows the reconstructions obtained when considering the 3.5–12 GHz band with a step of $5\Delta f$. These reconstructions have to be compared with the reconstructions presented in Fig. 8 (the whole frequency band), Fig. 10 (3.5–12 GHz band with a step of Δf), and Fig. A.3 (3.5–16 GHz band with a step of $5\Delta f$). Visually, these results seem to be of better quality than the reconstructions in Figs. 8 and A.3 given the reduction in perturbations around and in the centre of the object, and are similar to those presented in Fig. 10.

Let us compare the quantitative quality measures for these reconstructions, which are presented in the sixth row of Tables 2 and 3 and compare them with those in the second (the whole frequency band), third (3.5–12 GHz band with a step of Δf), and fifth rows (3.5–16 GHz band with a step of $5\Delta f$) of the same tables. $\mathrm{RMSE}^{\mathrm{all}}$, C^{ext}, and $\mathrm{RMSE}^{\mathrm{ext}}$ are not significantly different from those shown in the second row. However, C^{all} and C^{int} suggest that the reconstruction is superior when using the 3.5–12 GHz range with a $5\Delta f$ step, which is also the case for RO and $\mathrm{RMSE}^{\mathrm{void}}$. The values of these quantitative quality measures are very close to those shown in the third row. The same observation can be made when comparing these quantitative quality measures with those shown in the fifth row. From these observations, we can conclude that the reconstructions obtained using the 3.5–12 GHz range with a step of $5\Delta f$ offer a superior reconstruction quality compared to those obtained with the whole frequency band. This was expected given that the high frequencies were removed (see Sect. 6.3). Furthermore, the increase in the frequency step does not seem to influence the reconstruction quality. In the subsequent experiment, we therefore consider the 3.5–12 GHz range with a step of $5\Delta f$.

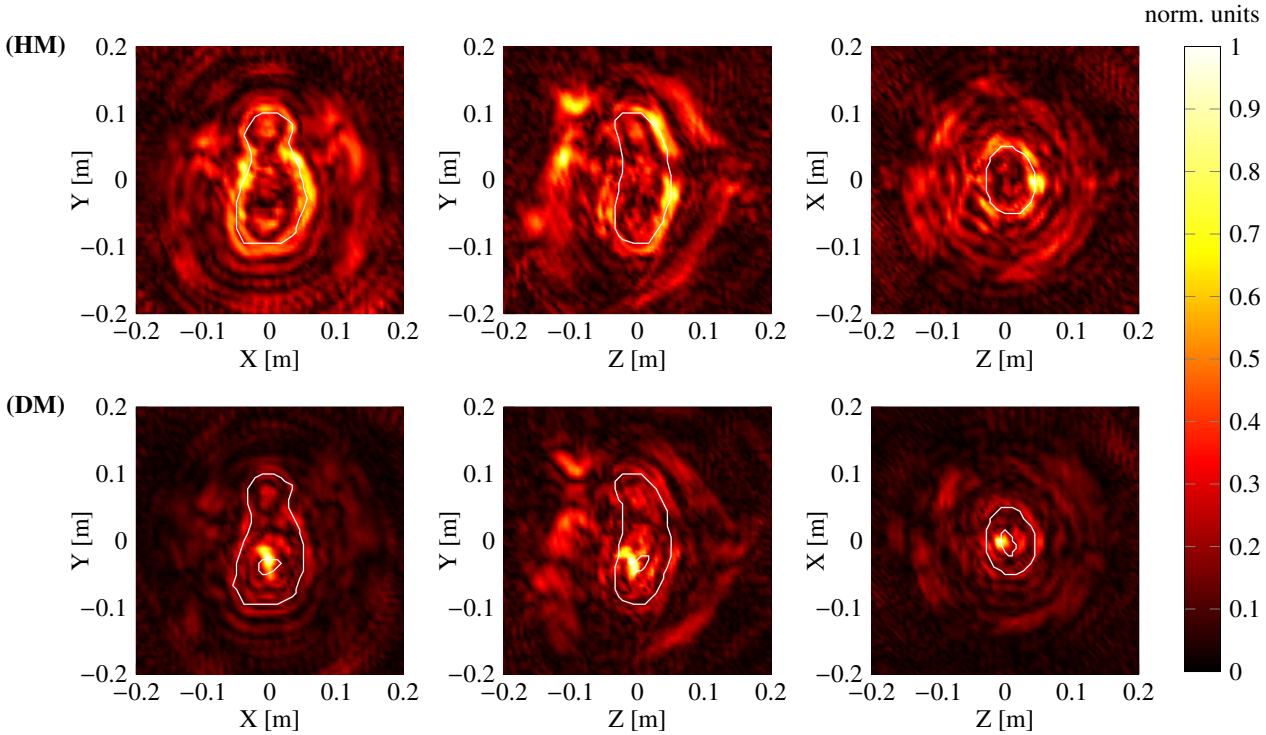

Fig. 12. Slices of the amplitude of the reconstructed induced currents using the PI method for both analogues considering the 3.5–12 GHz band and a step of $5\Delta f$ for 1257 quasi-monostatic positions. The line plot corresponds to the theoretical analogue. The figures on the left correspond to the plane Π_1, those in the middle to the plane Π_2, and those on the right to the plane Π_3 of Fig. 7.

6.6. Reduction in the number of quasi-monostatic pairs

As explained in Sect. 5.2, a reduction in the frequency band allows one to reduce the number of transmitter–receivers pairs. The 3.5–12 GHz band with a step of $5\Delta f$ corresponds to a spatial distribution of 1257 quasi-monostatic positions. The reconstructions using such parameters are shown in Fig. 12 and should be compared with those presented in Fig. 11 with all the quasi-monostatic positions. Examining these two figures, we do not observe major differences between the reconstructions.

The quantitative quality measures are therefore calculated and presented in the seventh row of Tables 2 and 3 and are to be compared with the measures on the sixth row of the tables. The results are again in good agreement, without significant differences. The similarity of the quantitative quality measures for the different reconstructions illustrates that it is not necessary to keep all transmitter–receiver pairs if the frequency band is reduced. In addition, the RO quantitative quality measure is slightly better in the case of the 1257 quasi-monostatic positions. We note that the number of n_v voxels taken into account for the RO calculation is small (n_v = 189) and is consequently influenced by even the slightest changes of very few voxels. With only 1257 quasi-monostatic position measurements and 35 frequencies, the quality of the reconstructions is not degraded. The difference between the reconstructions shown in Figs. 11 and 12 is presented in Fig. A.6 and confirms our above conclusions, as the maximum difference of intensity is very low (0.14) and no structure is distinguishable.

6.7. Influence of spatial configuration selection

As explained in Sect. 5.3, there are distinguishable effects of a larger angular step on the reconstructions. The reconstructions obtained using the sparse configuration of 363 points in Fig. A.4 are not accurate and neither the external shape nor the void are reconstructed. The quantitative quality measures are presented in the last row of Tables 2 and 3 and are to be compared with those obtained on the seventh rows of the tables. All quantitative quality measures except $\mathrm{RMSE}^{\mathrm{all}}$ and $\mathrm{RMSE}^{\mathrm{ext}}$ are inferior to those obtained with the 1257 quasi-monostatic positions. The improvement of the $\mathrm{RMSE}^{\mathrm{all}}$ and $\mathrm{RMSE}^{\mathrm{ext}}$, as explained in Sect. 6.2, is due to the fact that the signature of the external surface of the analogue is weakly reconstructed in the case of 363 points. Therefore, it does not accurately reflect the quality of the reconstruction, which is deteriorated. Here, we have under-sampled the angular step, which naturally leads to a degradation of the reconstructions since the Nyquist criterion is no longer respected.

7. Conclusions

Knowing the structure of SSSBs is of great importance for research concerning the history of the Solar System, and knowledge of their internal structure is key to understanding their formation and evolution. In this work, we focus on inverse methods for imaging two asteroids analogues, one of them containing a mantle and a deep interior void and the other being homogeneous. These inversion experiments were performed using multiple measurements using quasi-monostatic experimental data sets. This study, which proposes the processing of experimental data in the frequency domain, is a joint effort with another study that proposes processing in the time domain (Sorsa et al. 2023). The methods employed, that is, back-propagation and pseudo-inverse reconstructions, are simple, fast, and provide 3D maps of the induced current amplitude without the need for a reference field. Multiple quantitative quality measures were implemented and used to quantify the similarity between the reconstructed and the actual structure of the analogues.

The results show that the outer boundary of both asteroid analogues are clearly observed on the reconstructed maps. Moreover, the internal structure of these analogues can be reconstructed, that is, the inner core existing in the DM analogue is visible on the 3D maps. In addition, no significant differences are noticed between BP and PI methods.

In order to limit the number of required measurements, which is crucial in the case of a space mission, we carried out a study of the dependencies of both methods on the frequency band and on the number of transmitter–receiver pairs. We show that by using well-chosen parameters, it is possible to obtain equivalent reconstructions of the analogues while considerably reducing the necessary measurements and the computational cost. With only 1257 quasi-monostatic positions and 35 frequencies, the reconstructions are similar to those with 2372 positions and all the 250 frequencies from 3.5 to 16 GHz with a frequency step of 0.05 GHz. This amounts to taking only 53% of the initial set of measurements in positions and 14% of the frequencies. This new data set (1257 quasi-monostatic positions and 35 frequencies) allows a significant reduction in measurement time and an approximately 90% reduction in data processing time. Another potentially interesting result for space missions is that we are able to obtain relatively good reconstructions of the interior while maintaining a low level of uncertainty on the antenna–object distance. Moreover, we suggest that a significant reduction in the number of quasi-monostatic positions (less than 30% of the minimum number of measurements with respect to the Nyquist criterion) does not lead to satisfactory reconstructions without complementary data. This means that, to reconstruct the interiors of objects with this reduced set of measurements, it is important to take into account the available a priori information coming from other instruments on board the spacecraft, such as the asteroid shape or the mean effective permittivity of the asteroid.

The methods presented here have proven their ability to provide structural images and may be used to reconstruct the internal structure of SSSBs. In future work, we will focus on non-linear quantitative imaging, exploiting multiple scattering, allowing us to additionally obtain a permittivity map of such bodies.

Acknowledgement. Centre de Calcul Intensif d'Aix-Marseille is acknowledged for granting access to its high-performance computing resource. The authors acknowledge the opportunity provided by the Centre Commun de Ressources en Microonde to use its fully equipped anechoic chamber. L.-I. Sorsa, Y.O. Yusuf and S. Pursiainen were supported by Academy of Finland Centre of Excellence in Inverse Modelling and Imaging (2018–2025) and project 336151.

References

Bertero, M., & Boccacci, P. 1998, Introduction to Inverse Problems in Imaging (Bristol, UK; Philadelphia, Pa: Institute of Physics Publication)
Bevacqua, M. T., Crocco, L., Donato, L. D., & Isernia, T. 2017, IEEE Transac. Comput. Imaging, 3, 296
Bucci, O. M., & Isernia, T. 1997, Rad. Sci., 32, 2123
Campbell, S. L., & Meyer, C. D. 2009, Generalized Inverses of Linear Transformations (USA: Society for Industrial and Applied Mathematics)
Carry, B. 2012, Planet. Space Sci., 73, 98
Catapano, I., Crocco, L., & Isernia, T. 2008, IEEE Trans. Geosci. Remote Sens., 46, 3265
Ciarletti, V., Levasseur-Regourd, A. C., Lasue, J., et al. 2015, A&A, 583, A40
Ciarletti, V., Herique, A., Lasue, J., et al. 2017, MNRAS, 469, S805
Cloude, S. R., & Papathanassiou, K. P. 1998, IEEE Trans. Geosci. Remote Sens., 36, 15
Curlander, J., & McDonough, R. 1991, Synthetic Aperture Radar: Systems and Signal Processing, ed. K. J. S. (Hoboken: Wiley series in remote sensing)
de Berg, M., Cheong, O., van Kreveld, M., & Overmars, M. 2008, Computational Geometry: Algorithms and Applications (Berlin, Heidelberg: Springer Berlin Heidelberg)
Deng, J., Kofman, W., Zhu, P., et al. 2021a, IEEE Trans. Geosci. Remote Sens., 60, 1
Deng, J., Rogez, Y., Zhu, P., et al. 2021b, Comput. Phys. Commun., 265, 108002
Eyraud, C., Geffrin, J.-M., Sabouroux, P., et al. 2008, Rad. Sci., 43, 4
Eyraud, C., Litman, A., Herique, A., & Kofman, W. 2009, Inverse Prob., 26, 024005
Eyraud, C., Vaillon, R., Litman, A., Geffrin, J.-M., & Merchiers, O. 2013, J. Opt. Soc. Am. A, 30, 1967
Eyraud, C., Herique, A., Geffrin, J.-M., & Kofman, W. 2018, Adv. Space Res., 62, 1977
Eyraud, C., Sorsa, L.-I., Geffrin, J.-M., et al. 2020, A&A, 643, A68
Fujiwara, A., Kawaguchi, J., Yeomans, D. K., et al. 2006, Science, 312, 1330
Gassot, O., Herique, A., Fa, W., Du, J., & Kofman, W. 2021, Rad. Sci., 56, e07186
Geffrin, J.-M., Eyraud, C., Litman, A., & Sabouroux, P. 2009, Rad. Sci., 44, RS2007
Herique, A., Agnus, B., Asphaug, E., et al. 2018, Adv. Space Res., 62, 2141
Herique, A., Kofman, W., Zine, S., et al. 2019a, A&A, 630, A6
Herique, A., Plettemeier, D., Kofman, W., et al. 2019b, in 2019 EPSC-DPS joint meeting
Herique, A., Adell, P., Amini, R., et al. 2022 Europlanet Science Congress 2022, Granada, Spain, 18–23 Sep 2022, EPSC2022-474 https://doi.org/10.5194/epsc2022-474
Jutzi, M., & Benz, W. 2017, A&A, 597, A62
Kofman, W., Herique, A., Goutail, J.-P., et al. 2007, Space Sci. Rev., 128, 413
Kofman, W., Herique, A., Barbin, Y., et al. 2015, Science, 349, aab0639
Kramer, H. 2016, Hayabusa 2, Japan's Second Asteroid Sample Return Mission, Technical report, Eoportal
Litman, A., & Crocco, L. 2009, Inv. Prob., 26, 020201
Michel, P., Kueppers, M., Sierks, H., et al. 2018, Adv. Space Res., 62, 2261
Reigber, A., & Moreira, A. 2000, IEEE Trans. Geosci. Remote Sens., 38, 11
Saleh, H., Tortel, H., Leroux, C., et al. 2021, IEEE Trans. Antennas Propagation, 69, 983
Sava, P., & Asphaug, E. 2018a, Adv. Space Res., 62, 1146
Sava, P., & Asphaug, E. 2018b, Adv. Space Res., 61, 2198
Sorsa, L.-I., Takala, M., Bambach, P., et al. 2019, ApJ, 872, 44
Sorsa, L.-I., Takala, M., Eyraud, C., & Pursiainen, S. 2020, IEEE Trans. Comput. Imaging, 6, 579
Sorsa, L.-I., Eyraud, C., Herique, A., et al. 2021a, Mater. Design, 198, 109364
Sorsa, L.-I., Pursiainen, S., & Eyraud, C. 2021b, A&A, 645, A73
Sorsa, L.-I., Yusuf, Y. O., Dufaure, A., et al. 2023, A&A, 674, A73 (Paper II)
Tsuchiyama, A., Uesugi, M., Matsushima, T., et al. 2011, Science, 333, 1125
Ulander, L., & Frolind, P.-O. 1998, IEEE Trans. Geosci. Remote Sens., 36, 1540
Vaillon, R., & Geffrin, J.-M. 2014, J. Quant. Spectrosc. Radiat. Transf., 146, 100
Wendland, H. 2018, Numerical Linear Algebra An Introduction (Cambridge: Cambridge University Press)

Appendix A: Imaging results complementary figures

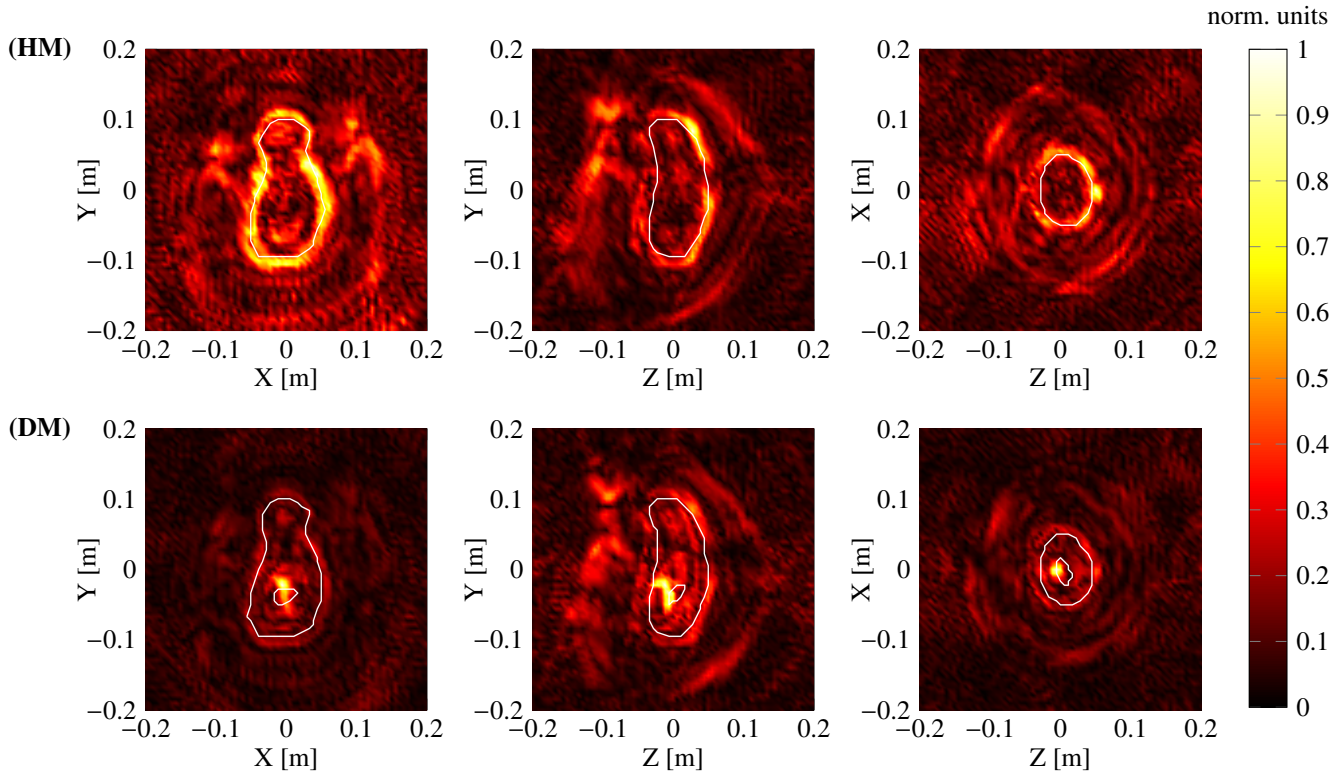

Fig. A.1: Slices of the amplitude of the reconstructed induced currents using the BP method for both analogues from measured scattered field considering the 3.5-16 GHz band and a step of Δf for 2372 quasi-monostatic positions. The line plot corresponds to the theoretical analogue. The figures on the left correspond to the plane Π_1, those in the middle to the plane Π_2, and those on the right to the plane Π_3.

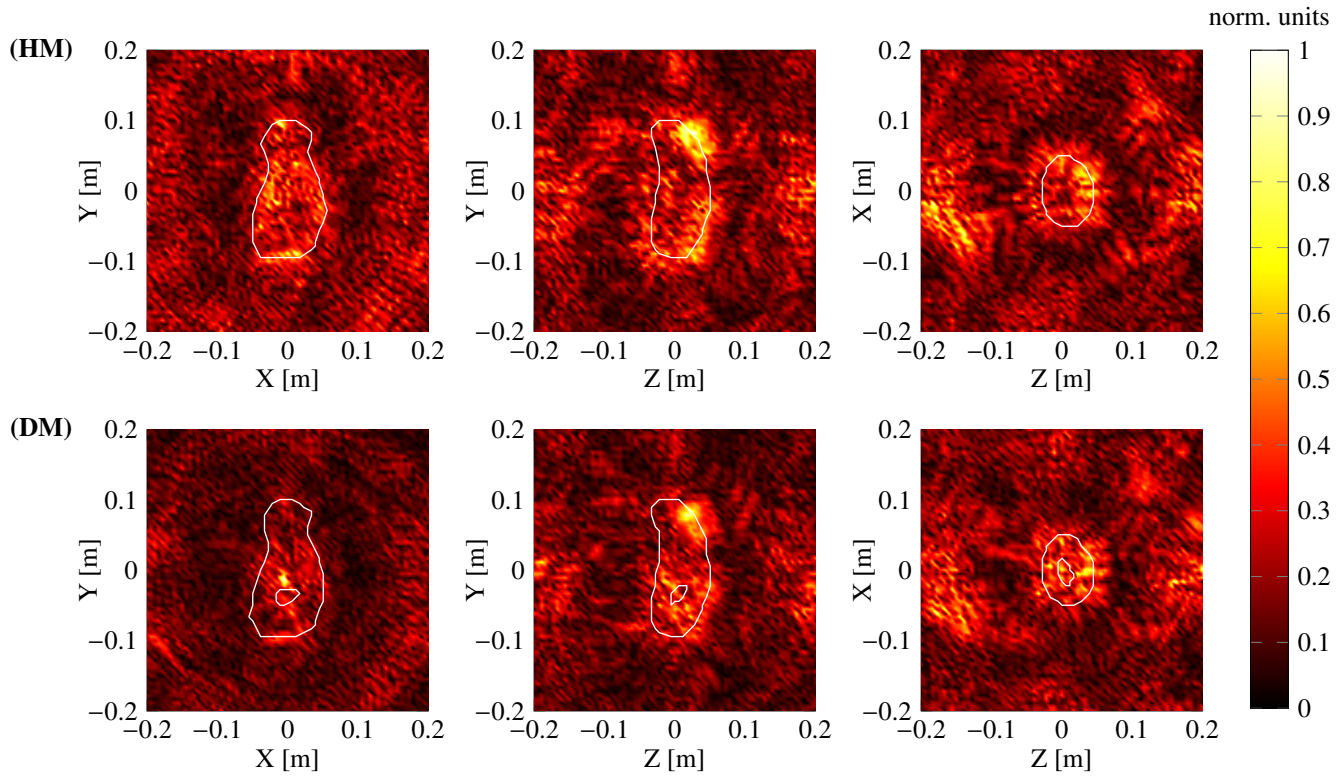

Fig. A.2: Slices of the amplitude of the reconstructed induced currents using **the PI** method for both analogues considering the 12-16 GHz band and a step of Δf for 2372 quasi-monostatic positions. The line plot corresponds to the theoretical analogue. The figures on the left correspond to the plane Π_1, those in the middle to the plane Π_2, and those on the right to the plane Π_3.

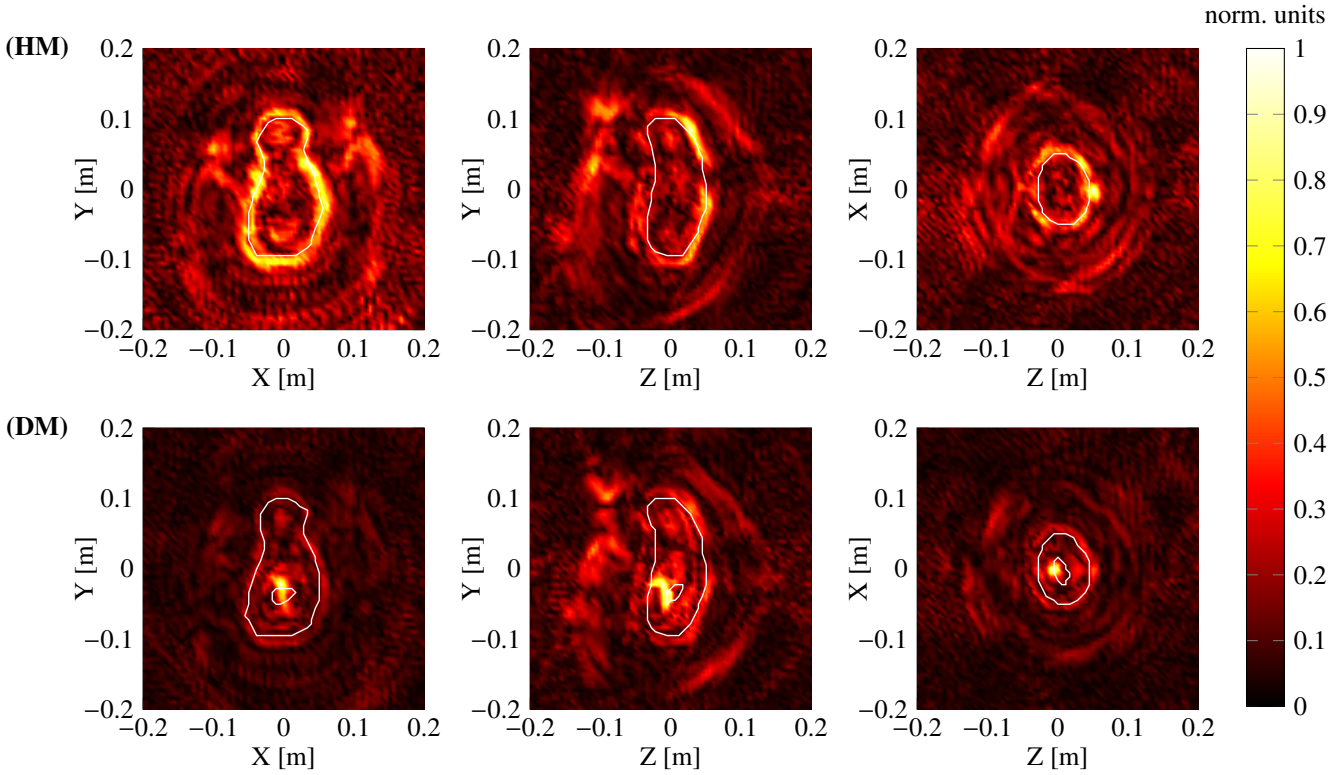

Fig. A.3: Slices of the amplitude of the reconstructed induced currents using **the PI** method for both analogues with 51 frequencies considering the 3.5-16 GHz band and a step of $5\Delta f$ for 2372 quasi-monostatic positions. The line plot corresponds to the theoretical analogue. The figures on the left correspond to the plane Π_1, those in the middle to the plane Π_2, and those on the right to the plane Π_3.

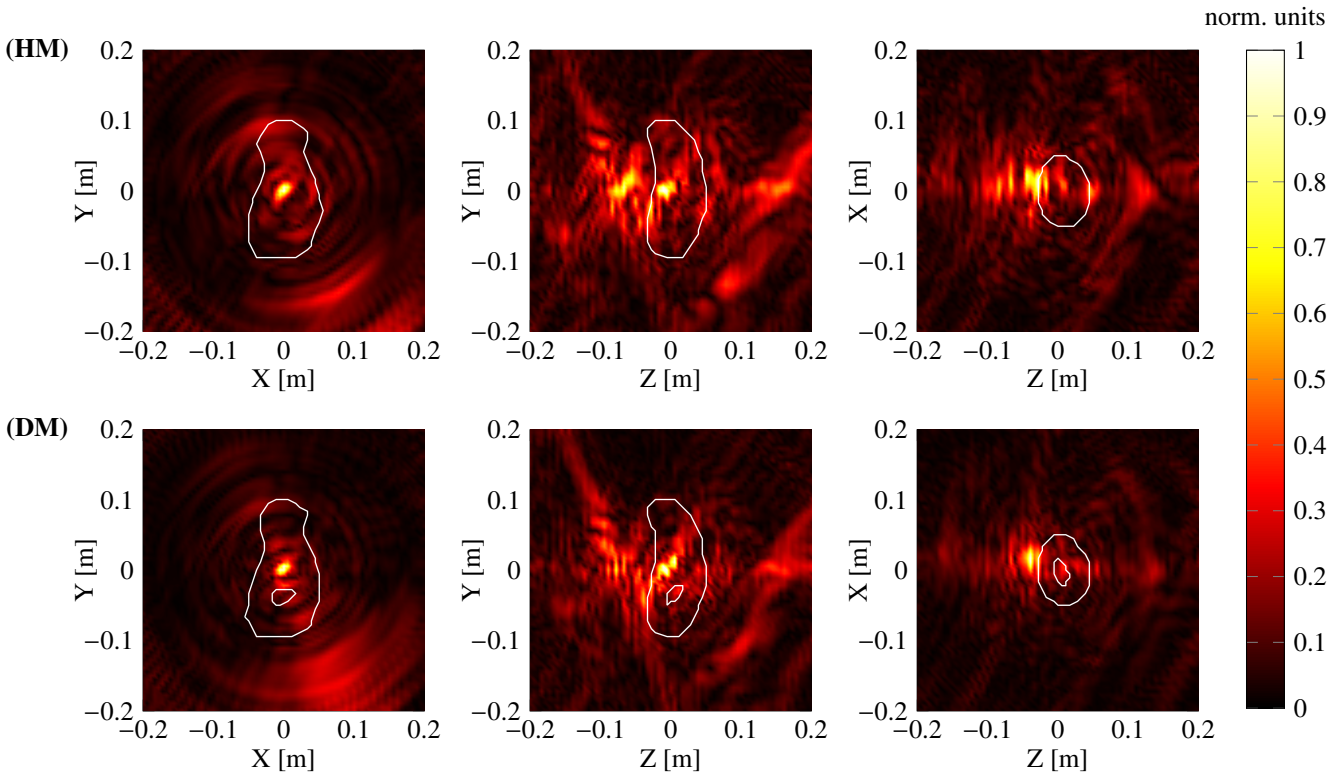

Fig. A.4: Slices of the amplitude of the reconstructed induced currents using **the PI** method for both analogues for the **363** configuration considering the 3.5-12 GHz band and a step of $5\Delta f$. The line plot corresponds to the theoretical analogue. The figures on the left correspond to the plane Π_1, those in the middle to the plane Π_2, and those on the right to the plane Π_3. The poor quality of reconstructions is mainly due to the low number of quasi-monostatic positions.

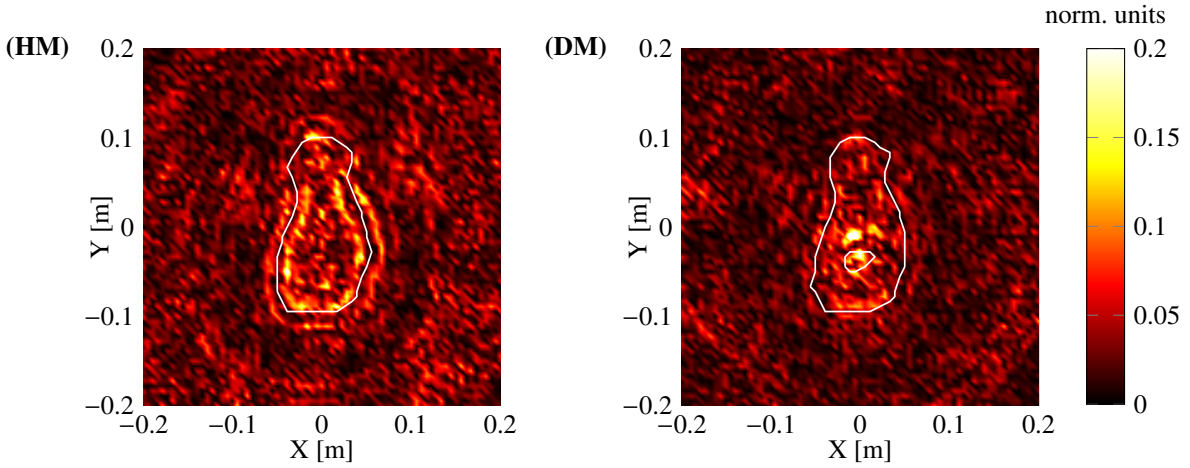

Fig. A.5: Slices of the difference between the amplitude of the induced current for the reconstruction considering the 3.5-16 GHz band (second row of Tables 2 and 3) and the reconstruction considering the 3.5-12 GHz band (third row of Tables 2 and 3) for both analogues and 2372 quasi-monostatic positions for each cases. The line plot corresponds to the theoretical analogue. The figures correspond to the plane Π_1. The frequency band is the determining factor here.

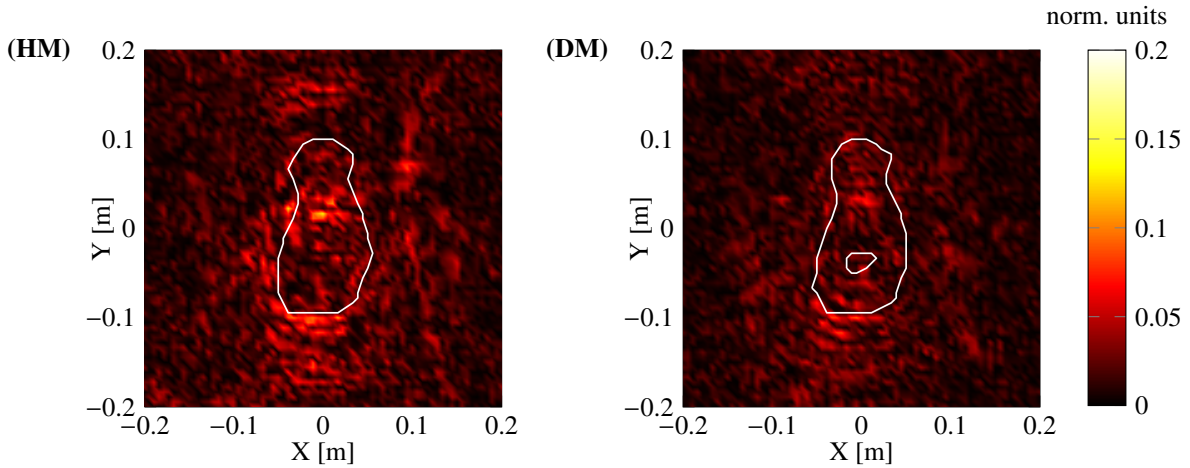

Fig. A.6: Slices of the difference between the amplitude of the induced current for the reconstruction considering the 3.5-12 GHz band with a step of $5\Delta f$ for 2372 quasi-monostatic positions (sixth row of Tables 2 and 3) and the reconstruction considering the 3.5-12 GHz band with a step of $5\Delta f$ for 1257 quasi-monostatic positions (Seventh row of Tables 2 and 3) for both analogues. The line plot corresponds to the theoretical analogue. The figures correspond to the plane Π_1. The number of quasi-monostatic positions is the determining factor here.